https://doi.org/10.1016/j.apenergy.2023.122030

A novel in-tube reformer for solid oxide fuel cell for performance improvement and efficient thermal management: a numerical study based on artificial neural network and genetic algorithm

Chen Wang[1], Qijiao He[1], Zheng Li[1], Idris Temitope Bello[1], Jie Yu[1], Keqing Zheng[1], Minfang Han[2,*], Meng Ni[1,*]

[1] Department of Building and Real Estate, Research Institute for Sustainable Urban Development (RISUD) and Research Institute for Smart Energy (RISE), The Hong Kong Polytechnic University, Hung Hom, Kowloon, Hong Kong, China
[2] Department of Energy and Power Engineering, Tsinghua University, Beijing, 100084, China

* Corresponding author:
Email: meng.ni@polyu.edu.hk (Meng Ni)
hanminfang@tsinghua.edu.cn (Minfang Han)

Abstract

The pursuit of higher power density and compact structure presents a critical challenge to the thermal management of solid oxide fuel cell. In this study, a novel in-tube reformer is proposed and a Multi-physics simulation-Artificial neural network-Multi-objective genetic algorism based optimization framework is developed to improve the output performance and reduce the internal temperature difference in solid oxide fuel cell. First, a validated multi-physics model is developed for parametric simulation and generating dataset. Afterwards, a surrogate model is obtained by training an artificial neural network to predict the output performance and internal temperature field of solid oxide fuel cell. Finally, multi-objective genetic algorithm optimizations based on the surrogate model are performed to maximize the output performance and minimize the internal temperature difference under different operation strategies. It is found that compared to the conventional configuration (without in-tube reformer), the use of in-tube reformer can effectively improve the electrochemical reactions, increase the fuel utilization (up to 34.2%) and current density (up to 14.5%) while significantly reducing the maximum temperature difference (up to 85.5%) in the cell, resulting in a uniform current density and temperature distribution along the cell. The proposed novel in-tube reformer and optimization framework are demonstrated to be highly powerful and can be easily applied to other fuel cell/electrolyzer systems to effectively improve system performance and realize efficient thermal management under actual demands.

Keywords

Solid oxide fuel cell; Internal reforming; Artificial neural network; Multi-objective genetic algorithm; Thermal management.

Nomenclature

Abbreviation

SOFC	Solid oxide fuel cell
ANN	Artificial neural network
MOGA	Multi-objective genetic algorism
PEN	Positive electrode/Electrolyte/Negative electrode
TPB	Triple phase boundary

Letter

R_i	Chemical reaction rate, $mol \cdot m^{-3} \cdot s^{-1}$
E_{act}	Activation energy, $J \cdot mol^{-1}$
E_{eq}	Equilibrium potential, V
ρ	Density, $kg \cdot m^{-3}$
γ_i	Pre-exponential factor
σ	Conductivity, $S \cdot m^{-1}$
T	Temperature, K
μ	Dynamic viscosity, $kg \cdot m^{-1} \cdot s^{-1}$
R	Universal gas constant, 8.314 $J \cdot mol^{-1} \cdot K^{-1}$
ε	Porosity
ϕ	Electrostatic potential, V
F	Faraday constant, 96485.3 $C \cdot mol^{-1}$
k	Permeability, m^2
y_i	Molar fraction of specie i
λ_{eff}	Effective thermal conductivity, $W \cdot m^{-1} \cdot K^{-1}$
ΔH^0	Enthalpy change, $J \cdot mol^{-1}$
ΔS^0	Entropy change, $J \cdot mol^{-1} \cdot K^{-1}$
f_i	Fugacity of specie i, Pa
$D_{ij,eff}$	Effective binary diffusion coefficient, $m^2 \cdot s^{-1}$
$D_{ik,eff}$	Effective Knudsen diffusion coefficient, $m^2 \cdot s^{-1}$
c_p	Specific heat capacity, $J \cdot mol^{-1} \cdot K^{-1}$
Q_i	Heat source term, $W \cdot m^{-3}$
τ	Tortuosity

1 Introduction

As a novel energy conversion device, solid oxide fuel cell (SOFC) is attracting increasing attention [1]. Since the chemical energy in the fuels can be directly converted into electricity without combustion and mechanical processes, the thermal efficiency of SOFC is not limited by the Carnot cycle and can reach over 70% [2]. Meanwhile, the high temperature operation, no moving components, and modularity features make SOFC have the advantages of excellent fuel flexibility, long-term stability, low pollution, and high capacity flexibility [1,2]. At present, SOFC has been used to provide electricity for civil, commercial, transportation and other fields, which is important for alleviating energy crisis, meeting power demand and reducing environmental pollution [2].

Currently, one challenge of SOFC is to improve power density and increase compactness [3-7]. With continued efforts, the power density of SOFC has exceeded $1 W \cdot cm^{-2}$ [4] and has been used in ships [8], vehicles [9] and drones [10]. However, the pursuit of high power density and compact size of SOFC operating at high temperature also brings a series of thermomechanical and stability problems [11]. This is because the heat generated by the intense and uneven electrochemical reactions in SOFC can lead to significant thermal stress, which may cause electrolyte fracture and delamination between electrolyte and electrode, thus significantly affecting the cell performance and reducing the lifetime [11]. When internal reforming schemes are adopted to further increase compactness and improve thermal efficiency of the system, the spatial and intensity mismatch between the intense heat-absorbing chemical reactions at the upstream region and the exothermic electrochemical reactions in the downstream region can further enhance the temperature gradient in the SOFC, leading to more severe thermal stresses [11]. According to reports, the temperature gradients in SOFCs without thermal management measures can reach $20 K \cdot cm^{-1}$[12,13], and it can further exceed $50 K \cdot cm^{-1}$ [14,15] with internal reforming, which all apparently exceed the allowable value of $10 K \cdot cm^{-}$

[1] [16].

To address the thermomechanical and stability problems caused by thermal stresses in SOFC, novel composite electrode materials have been developed to balance the thermal stresses caused by temperature differences [17-20]. Zhang et al. [19] demonstrated a novel thermal expansion offset approach to develop high performance and durable cathode. By mixing Co-containing cathode materials and oxides with a negative thermal expansion coefficient (TEC), they successfully reduced the TEC of the composite cathode, which is close to that of the electrolyte. As the TEC mismatch is eliminated, they achieved both high performance and excellent durability of SOFC. Apart from material development, appropriate thermal management methods are also effective solutions to reduce the thermal stress in SOFC and improve the operating lifetime [21-30]. Typically, the most common thermal management method for SOFC is to supply excess air to the cathode channel, but the additional airflow obviously increases the system operating cost and reduces the system efficiency [22,26,31]. Therefore, researchers have developed various novel approaches for thermal management of SOFC, including optimizing the flow arrangement [21,22], developing novel interconnectors [23], integrating heat pipes [24,25], using chemical coolers [26], and rearranging catalyst distribution [28-30]. Recknagle et al. [21] found that the co-flow arrangement has the most uniform temperature distribution and the smallest thermal gradient compared to counter-flow and cross-flow, and has more thermal structural advantages. Guo et al. [23] developed a novel cathode interconnector with discrete ribs and found that the novel design can increase the power density by up to 12.96% while reducing the thermal stress of the interconnector by 19.31% and lowering the failure probability of the cell by up to 28.97%. Dillig et al. [24] Integrated the planar liquid sodium heat pipe into the interconnector to reduce the internal temperature gradient of SOFC. It was found that for a SOFC stack with an effective area of 200×200 mm^2, the maximum temperature difference within the cell layer could be reduced from 296 K to 189

K by using the heat pipe interconnector, and it could be further reduced to 50 K by increasing the number of heat pipe interconnect layers. Promsen et al. [27] used saturated water for thermal management of SOFCs and found that the use of water cooling can reduce the temperature difference from 295 K to 62 K for tubular SOFC and from 185 K to 26 K for planar SOFC compared to the conventional air cooling method, thus reducing the parasitic air supply power.

The cooling effect of the SOFC thermal management scheme is directly determined by the structural and operating parameters in the system. Nevertheless, the experience-based optimization of output performance and cooling effects is limited, so the advanced algorithms have also been used to assist the SOFC optimization [32-36]. Artificial neural network (ANN) is a computational model that simulates the operating characteristics of biological neural systems and is suitable for seeking complex nonlinear relationships between the inputs and outputs [37]. Genetic algorithm (GA) is an optimization search algorithm proposed by adapting the principles of biological evolution [38]. Numerous studies have been conducted to demonstrate the effectiveness and efficiency of combining ANN and GA with multi-physics simulations [32-36]. Yan et al. [33] established a prediction model for cathode overpotential and degradation rate using ANN, and obtained the optimal SOFC microstructure with low cathode overpotential and degradation rate through multi-objective genetic algorithm (MOGA), thus optimizing the process parameters. Xu et al. [35] used CFD modeling, ANN and GA to improve the output performance of SOFC. It was found that among 19 widely used intelligent algorithms, ANN can provide the best prediction accuracy, and the power density of SOFC can be improved by 97% after GA optimization. Wang et al. [36] developed a predictive model for the output performance and carbon deposition characteristics of SOFC using deep neural networks (DNN). They obtained the optimal electrode microstructure using multi-objective genetic algorithm (MOGA) optimization to get higher power density and significantly reduce the carbon deposition rate.

As can be seen, although the current thermal management schemes in SOFC can take away the excess heat from the cell and reduce the thermal stress caused by large temperature gradient, this part of heat is not used by the system, resulting in the loss of overall system thermal efficiency [27]. Meanwhile, the complex and heavy cooling structures make it difficult for the fabrication and miniaturization of SOFC [23,24], and the reported novel cooling structures are also insufficient to achieve the optimal cell performance and precise control of internal temperature. In this study, a novel in-tube reformer is proposed, and an optimization framework is developed to improve the output performance and reduce the temperature difference in SOFC. The in-tube reformer can fully utilize the excess heat and reduce the temperature difference inside the cell. And the framework combines multi-physics simulation (MPS), artificial neural network (ANN) and multi-objective genetic algorithm (MOGA) optimization. The experimentally validated multi-physics model fully considers the fluid flow, species transfer, chemical/electrochemical reactions and thermal effects in the SOFC. A database is established based on the Latin hypercube sampling (LHS) method by considering the effects of structural (size of inner tube, thickness of reforming layer) and operating (anode flow rate, anode gas composition) parameters of the system. A numerical surrogate model of the multi-physical model is obtained by training the ANN. Finally, the trade-offs among the system average temperature, positive electrode/electrolyte/negative electrode (PEN) maximum temperature difference, current density, and syngas production are obtained using the MOGA. The optimization results can improve the system performance while achieving efficient thermal management of SOFC (eliminating temperature difference and operating in thermal neutrality). The proposed MPS, ANN and MOGA based optimization framework using in-tube reformer can increase the power density while minimizing the PEN temperature difference, but also features simple structure and easy fabrication, which can facilitate the miniaturization and commercialization of SOFC.

2 Methodology

2.1 Physical model and optimization framework

The scheme of the tubular SOFC with a novel in-tube reformer is demonstrated in Fig. 1(a). The anode-supported SOFC is adopted for co-production of electricity and syngas. The SOFC uses glycerol as fuel and adopts an internal reforming scheme with a co-flow configuration for the anode channel and cathode channel. YSZ, Ni/YSZ, and LSM/YSZ are used as the electrolyte, anode and cathode, with a thickness of 10μm, 600μm, and 100μm, respectively. In the anode channel, a stainless-steel tube is used to supply fuel (glycerol+H_2O) to the system, and a 400μm thick internal reforming layer (porous medium with uniformly distributed Ni-Al_2O_3 catalyst for glycerol reforming) is arranged inside the tube to improve the fuel conversion and to match the heat absorption/release of the chemical/electrochemical reactions. Because of the strong inlet effect and the small size, the chemical and electrochemical reactions at the bottom of the tubular SOFC (also the anode corner) are not considered. The detailed structural dimensions and material properties are listed in Table 1.

Fig. 1(b) illustrates the optimization workflow combining MPS-ANN-MOGA. First, the multi-physics processes in SOFC are considered comprehensively to develop the MPS model. Afterwards, the validated model is used to perform the parametric studies and to build the database for ANN training. The well-trained ANN model can accurately represent the complex nonlinear relationship of input and output to obtain the surrogate model. Finally, the optimal structural design and operating parameters of the cell are obtained by integrating MOGA optimization, so as to maximize the performance and minimize the temperature difference in the SOFC.

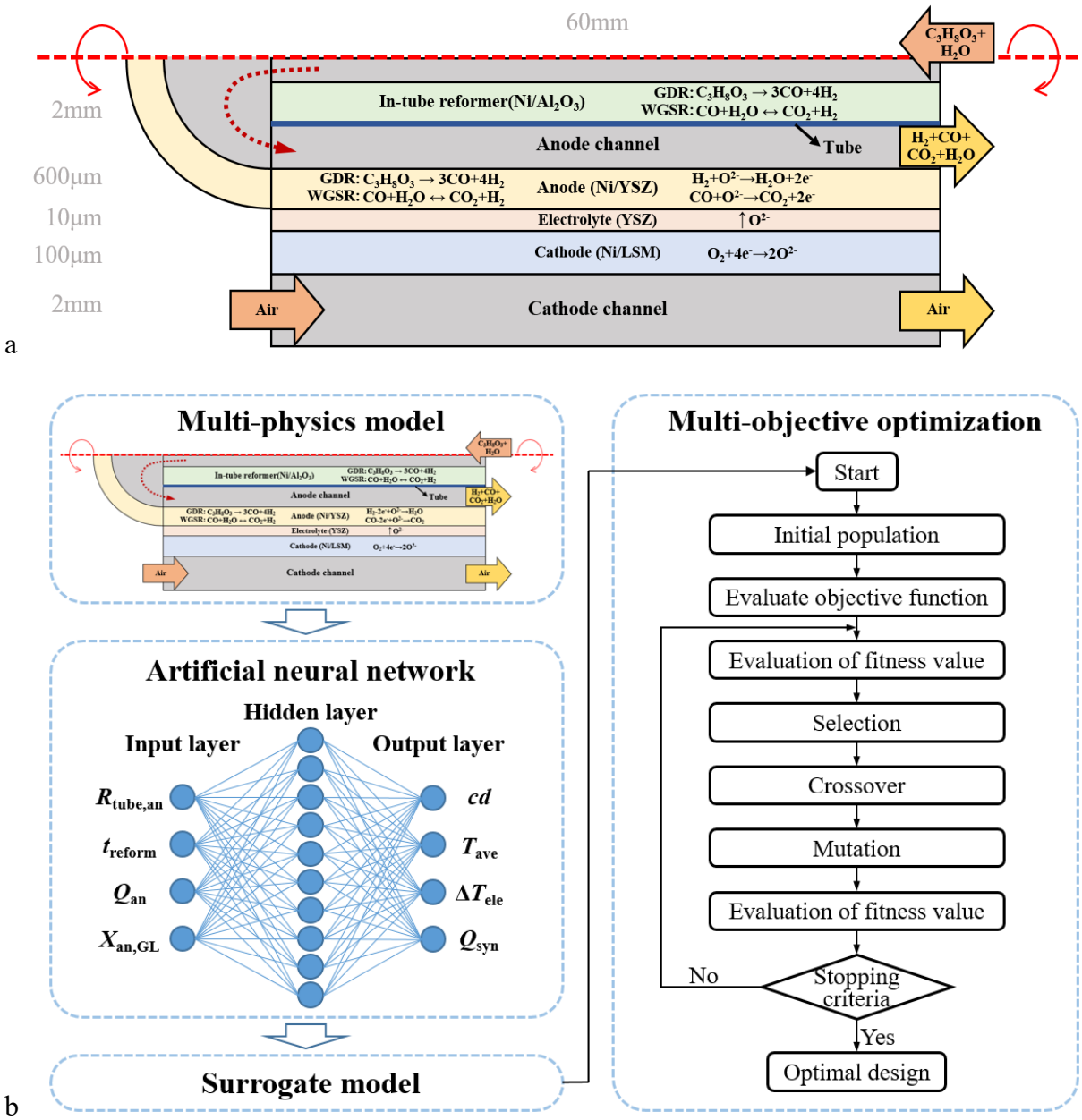

Fig.1 (a) Tubular glycerol-fueled SOFC with novel in-tube reformer; (b) The workflow for optimization combining MPS-ANN-MOGA

Table 1 Structural dimensions and material properties [39-42]

Materials or Parameters	Expression or Value	Unit
Conductivity		
Ni	3.27×10^{6}-$1065.3\times T$	$S\cdot m^{-1}$
YSZ	$3.34\times10^{4}\times\exp(-10300\times T^{-1})$	$S\cdot m^{-1}$

LSM	$4.2\times10^{7}/T\times\exp(-1150\times T^{-1})$	$S\cdot m^{-1}$
Dimensions		
Length of cell	62.6	mm
Length of anode tube	60	mm
Anode channel	2.0	mm
Cathode channel	2.0	mm
Thickness of anode tube	0.1	mm
Inner radius of anode tube	1.0~1.6	mm
Thickness of in-tube reformer	200~1000	μm
Anode	600	μm
Cathode	100	μm
Electrolyte	10	μm
Tortuosity	3	-
Porosity		
Anode	0.4	-
Cathode	0.4	-
In-tube reformer	0.4	-
Permeability		
Anode	1.76×10^{-11}	m^2
Cathode	1.76×10^{-11}	m^2
In-tube reformer	1.76×10^{-11}	m^2
S_{TPB}		
Anode	2.66×10^{5}	$m^2\cdot m^{-3}$
Cathode	3.33×10^{5}	$m^2\cdot m^{-3}$
α		

	α_{an}	0.5	-
	α_{ca}	0.5	-
γ			
	$\gamma_{an,H2}$	1.5×10^{9}	-
	$\gamma_{ca,H2}$	7×10^{8}	-
E_{act}			
	$E_{act,an}$	1.2×10^{5}	$J\cdot mol^{-1}$
	$E_{act,ca}$	1.3×10^{5}	$J\cdot mol^{-1}$

The anode and cathode channels are in a co-flow configuration. During operation, air is passed into the cathode channel, while a mixture of glycerol and H_2O is supplied into the anode stainless-steel tube. The glycerol steam reforming (GSR, Eq. (1)) in the anode will be catalyzed by Ni-based catalyst to undergo glycerol decomposition reaction (GDR, Eq. (2)) and water gas shift reaction (WGSR, Eq. (3)) to produce H_2 and CO. The produced H_2 and CO will then participate in the electrochemical reactions (Eqs. (4), (5)) at the anode, releasing electrons at the anode triple phase boundary (TPB) and reacting with O^{2-} transferred from the cathode to produce H_2O and CO_2. The released electrons will flow through the external load and reach the cathode, where they will react with O_2 at the cathode TPBs to produce O^{2-} (Eq. (6)), which will be continuously transferred to the anode through the oxygen-ion conducting electrolyte (YSZ) under the effect of potential difference, thus completing the circuit. Since the methane formation reaction (Eqs. (7), (8)) on the Ni-based catalyst requires low temperature and high pressure conditions [43], it is not considered since it is not thermodynamically favorable in the SOFC. Moreover, the experiment exhibited 49 hours of stable operation with no notable carbon formation [44], so the possible carbon deposition reactions (Eqs. (9), (10)) are also not considered.

$$C_3H_8O_3 + 3H_2O \rightarrow 3CO_2 + 7H_2, \Delta H_{298K} = 128 kJ/mol \quad (1)$$

$$C_3H_8O_3 \rightarrow 3CO + 4H_2, \Delta H_{298K} = 251 kJ/mol \quad (2)$$

$$CO + H_2O \leftrightarrow CO_2 + H_2, \Delta H_{298K} = -41 kJ/mol \quad (3)$$

$$H_2 + O^{2-} \rightarrow H_2O + 2e^- \quad (4)$$

$$CO + O^{2-} \rightarrow CO_2 + 2e^- \quad (5)$$

$$O_2 + 4e^- \rightarrow 2O^{2-} \quad (6)$$

$$CO_2 + 4H_2 \leftrightarrow CH_4 + 2H_2O, \Delta H_{298K} = -164 kJ/mol \quad (7)$$

$$CO + 3H_2 \leftrightarrow CH_4 + H_2O, \Delta H_{298K} = -206 kJ/mol \quad (8)$$

$$CO(g) + H_2(g) \leftrightarrow H_2O(g) + C(s), \Delta H_{298K} = -131 kJ/mol \quad (9)$$

$$2CO(g) \leftrightarrow CO_2(g) + C(s), \Delta H_{298K} = -171 kJ/mol \quad (10)$$

The reforming of glycerol is highly heat absorbing (Eq. (1)) while the H_2 and CO electrochemical reactions are highly exothermic. Therefore, when the structural parameters of the cell are determined, it is possible to match the heat absorption from chemical reactions with the heat release from electrochemical reactions by adjusting the size of anode reformer and operating parameters to reduce the PEN temperature difference within the cell. Meanwhile, since the internal reforming scheme is adopted in this study, the excess heat inside the cell is not discharged and wasted, but is utilized by the glycerol reforming process, thus preventing the loss of overall system thermal efficiency due to heat waste. Besides, compared with the complex thermal management structures, the thermal management scheme (in-tube reformer) in this study has the advantages of simple structure and easy fabrication. The following assumptions are employed in this study:

(1) The gases are incompressible and ideal.

(2) The active sites are homogeneous for the chemical/electrochemical reactions.

(3) Heat radiation, carbon deposition, and methane formation are not considered.

(4) Only O_2, H_2 and CO will react electrochemically.

(5) The electronic/ionic conducting phase is uniformly distributed and continuous.

2.2 Chemical model

At the in-tube reforming layer and the anode electrode, glycerol is converted to H_2 and CO in the presence of Ni-based catalysts through the main reactions of glycerol decomposition reaction (GDR, Eq. (2)) and water gas shift reaction (WGSR, Eq. (3)). The reaction rates of GDR and WGSR ($mol \cdot m^{-3} \cdot s^{-1}$) can be expressed as:

GDR [41]:

$$R_{GDR} = 0.036 e^{\frac{-63300}{RT}} p_{C_3H_8O_3}^{0.253} p_{H_2O}^{0.358} A_{\text{metal surface}} \tag{11}$$

WGSR [41]:

$$R_{WGSR} = 0.0171 e^{\frac{-103196}{RT}} \left(p_{H_2O} p_{CO} - \frac{p_{H_2} p_{CO_2}}{K_{ps}} \right) \tag{12}$$

$$K_{ps} = \exp(-0.2935 Z^3 + 0.6351 Z^2 + 4.1788 Z + 0.3169) \tag{13}$$

$$Z = \frac{1000}{T} - 1 \tag{14}$$

where T is reacting temperature, K; R is gas constant, 8.314 $J \cdot mol^{-1} \cdot K^{-1}$; p_i is the partial pressure of specie i, Pa; $A_{\text{metal surface}}$ is metal surface area of the catalyst, $m^2 \cdot m^{-3}$.

2.3 Electrochemical model

In operation, the operating potential (V) is represented as:

$$V = E - \eta_{act,an} - \eta_{act,ca} - \eta_{ohmic} \tag{15}$$

where E represents the equilibrium potential, V; η_{act} represents the activation overpotential, V; η_{ohmic} represents the ohmic overpotential, V.

The Nernst equation is implemented to calculate the equilibrium potential E [39,41]:

$$E_{H_2} = E_{H_2}^0 + \frac{RT}{2F} \left(\frac{p_{H_2} (p_{O_2})^{0.5}}{p_{H_2O}} \right) \tag{16}$$

$$E_{\mathrm{CO}}=E_{\mathrm{CO}}^{0}+\frac{RT}{2F}\left(\frac{p_{\mathrm{CO}}(p_{\mathrm{O_2}})^{0.5}}{p_{\mathrm{CO_2}}}\right) \tag{17}$$

where F is the Faraday constant; E_{H2}^{0} and E_{CO}^{0} are the standard cell potentials (V), which are temperature dependent and can be further expressed as [39,41]:

$$E_{\mathrm{H_2}}^{0}=1.253\text{-}0.00024516T \tag{18}$$

$$E_{\mathrm{CO}}^{0}=1.46713\text{-}0.0004527T \tag{19}$$

The relationship between activation overpotential (η_{act}) and current density (i) is described by using the Butler-Volmer (BV) equation [39,41]:

$$i=i_0\left[\exp\left(\frac{\alpha nF\eta_{\mathrm{act}}}{RT}\right)-\exp\left(\frac{-(1-\alpha)nF\eta_{\mathrm{act}}}{RT}\right)\right] \tag{20}$$

where α is the electron transfer coefficient; n is the number of electrons transferred per reaction. And i_0 is the exchange current density ($\mathrm{A\cdot m^{-2}}$), which can be further calculated for the H_2/H_2O electrochemical reaction as [40,42]:

$$i_{0,\mathrm{an},\mathrm{H_2}}=\gamma_{\mathrm{an},\mathrm{H_2}}\cdot p_{\mathrm{H_2},\mathrm{an}}^{\mathrm{TPB}}\cdot\exp\left(-\frac{E_{\mathrm{act,an}}}{RT}\right) \tag{21}$$

$$i_{0,\mathrm{ca},\mathrm{H_2}}=\gamma_{\mathrm{ca},\mathrm{H_2}}\cdot\left(p_{\mathrm{O_2},\mathrm{ca}}^{\mathrm{TPB}}\right)^{0.21}\cdot\exp\left(-\frac{E_{\mathrm{act,ca}}}{RT}\right) \tag{22}$$

where $\gamma_{\mathrm{an,H2}}$ and $\gamma_{\mathrm{ca,H2}}$ represent the pre-expontential factors for the anode and cathode sides, respectively; $p_{\mathrm{H2,an}}^{\mathrm{TPB}}$ is the partial pressure of H_2 at the anode TPBs, Pa; $E_{\mathrm{act,an}}$ and $E_{\mathrm{act,ca}}$ are the activation energy for the anode and cathode, respectively, $\mathrm{J\cdot mol^{-1}}$.

As for the electrochemical reaction of CO/CO_2, since the reaction rate of H_2 is observed to be 2.2 times of that of CO in the experiment [45], it is assumed in this study that the exchange current density of CO satisfies the relationship of [41,45]:

$$i_{0,\mathrm{an},\mathrm{CO}}=\frac{1}{2.2}\cdot i_{0,\mathrm{an},\mathrm{H_2}} \tag{23}$$

In addition, the oxygen-ions/electrons transfer process in the electrode and electrolyte is

calculated using the Ohm's law:

$$i_{\mathrm{oi}} = -\sigma_{\mathrm{oi,eff}} \nabla\left(Ø_{\mathrm{oi}}\right) \tag{24}$$

$$i_{\mathrm{e}} = -\sigma_{\mathrm{e,eff}} \nabla\left(Ø_{\mathrm{e}}\right) \tag{25}$$

where Ø represents the conducting potential; $\sigma_{\mathrm{oi,eff}}$ and $\sigma_{\mathrm{e,eff}}$ represent the effective conductivity of oxygen-ions (oi) and electrons (e) in porous electrodes, respectively, which is related to the tortuosity (τ) and volume fraction of oxygen-ion/electron phase in the electrodes as:

$$\sigma_{\mathrm{oi,eff}} = \sigma_{\mathrm{oi}} \frac{V_{\mathrm{oi}}}{\tau_{\mathrm{oi}}} \tag{26}$$

$$\sigma_{\mathrm{e,eff}} = \sigma_{\mathrm{e}} \frac{V_{\mathrm{e}}}{\tau_{\mathrm{e}}} \tag{27}$$

2.4 Mass and momentum transport

The gas flow and momentum transport processes in porous medium and gas channels can be simulated through Navier-Stokes (N-S) equation [42]:

For gas channels, the N-S equation is:

$$\rho \frac{\partial u}{\partial t} + \rho u \nabla u = -\nabla p + \nabla \left[\mu \left(\nabla u + \left(\nabla u \right)^T \right) - \frac{2}{3} \mu \nabla u \right] \tag{28}$$

For porous medium (electrodes and in-tube reforming layer), the N-S equation containing the Darcy's term is:

$$\rho \frac{\partial u}{\partial t} + \rho u \nabla u = -\nabla p + \nabla \left[\mu \left(\nabla u + \left(\nabla u \right)^T \right) - \frac{2}{3} \mu \nabla u \right] - \frac{\varepsilon \mu u}{k} \tag{29}$$

where k is permeability, m^2; ρ is gas density, $\mathrm{kg \cdot m^{-3}}$; ε is porosity; u is velocity vector, $\mathrm{m \cdot s^{-1}}$; μ is dynamic viscosity, $\mathrm{kg \cdot m^{-1} \cdot s^{-1}}$. In the steady-state simulations in this study, the transient terms in Eqs. (28), (29) are treated as 0. ρ and μ for the gas mixture can be further expressed as:

$$\rho = \sum_{i=1}^{N} y_i \rho_i \tag{30}$$

$$\mu = \sum_{i=1}^{N} y_i \mu_i \tag{31}$$

where ρ_i, μ_i and y_i are the density, dynamic viscosity, and molar friction of specie i, respectively.

The species diffusion process in gas channels (molecular diffusion) as well as porous electrodes/reforming layer (molecular diffusion and Knudsen diffusion) are simulated by using the general Fick model [46]:

$$N_i = -\frac{1}{RT}\left(\frac{k y_i P}{\mu}\frac{\partial P}{\partial z} - D_{ij,\text{eff}}\frac{\partial\left(y_i P\right)}{\partial z}\right) \tag{32}$$

where k is permeability, m^2; y_i is the molar fraction of specie i; $D_{ij,\text{eff}}$ represents the effective binary diffusion coefficient, which can be further calculated as [47]:

$$D_{ij,\text{eff}} = \frac{\varepsilon}{\tau}\left(\frac{1}{D_{ij}} + \frac{1}{D_{ik}}\right)^{-1} \tag{33}$$

$$D_{ij} = \frac{0.00143T^{1.75}}{2p\left(v_i^{1/3} + v_j^{1/3}\right)^2}\left(\frac{1}{M_i} + \frac{1}{M_j}\right)^{1/2} \tag{34}$$

$$D_{ik} = \frac{2}{3} r \sqrt{\frac{8RT}{\pi M_i}} \tag{35}$$

where D_{ij} is the binary diffusion coefficient, $m^2 \cdot s^{-1}$; D_{ik} is the effective Knudsen diffusion coefficient, $m^2 \cdot s^{-1}$; M_i is the molar mass of species i, $kg \cdot mol^{-1}$; r is the radius of electrode pores, m; v is special molecule diffusion volume of each species, m^3. The detailed material properties can be found in Ref. [48-52].

2.5 Heat transfer

During operation, the uneven and intense chemical/electrochemical reactions within the cell can lead to complex internal temperature conditions, which can not only seriously affect the performance of the cell, but can even cause obvious thermal stress and result in the failure of cell structure. The heat generate/transfer and temperature distribution in the cell are simulated by general heat balance equation [42]:

In channels:

$$\rho c_p u \cdot \nabla T + \nabla \cdot \left(-\lambda_g \nabla T\right) = 0 \tag{36}$$

In porous electrodes/reforming layer and electrolyte:

$$\rho c_p u \cdot \nabla T + \nabla \cdot \left(-\lambda_{eff} \nabla T\right) = Q \tag{37}$$

$$\lambda_{eff} = \left(1-\varepsilon\right)\lambda_s + \varepsilon\lambda_g \tag{38}$$

where c_p represents the specific heat capacity, $J \cdot mol^{-1} \cdot K^{-1}$; λ_g and λ_s represent the thermal conductivity ($W \cdot m^{-1} \cdot K^{-1}$) of gas species and solid phase, respectively. Q is the heat source term ($W \cdot m^{-3}$), describing the heat releasing/absorbing processes that occur at the electrodes, electrolyte, and reforming layer during operation. Heat source terms caused by ohmic loss, chemical reactions, and electrochemical reactions are calculated as [42]:

$$Q_{ohmic} = -\left(i \cdot \nabla \varphi\right) \tag{39}$$

$$Q_{chem} = R_{chem} \cdot \Delta H_{chem} \tag{40}$$

$$Q_{elec} = \left(-T\Delta S\right) \cdot \frac{i}{nF} \tag{41}$$

where R_{chem} represents the reaction rate of each chemical reaction; ΔH_{chem} indicates the enthalpy change in each chemical reaction; ΔS indicates the entropy change in each electrochemical reaction. The physical properties of each gas and solid material can be found in Ref. [41,48,49,53].

2.6 Boundary conditions

The 2D steady multi-physics model in this study is solved using the finite element method (COMSOL Multiphysics), and the boundary conditions used are listed in Table 2.

Table 2 Boundary conditions in this study

Location	Boundary conditions
Anode/Anode channel interface	Ø=0

Cathode/Cathode channel interface	$Ø=V_{cell}$
Anode tube inlet	Specify the temperature, flow rate, and gas composition
Cathode channel inlet	Specify the temperature, flow rate, and gas composition
Anode channel outlet	Pressure outlet
Cathode channel outlet	Pressure outlet
Other surfaces	Insulated and adiabatic

2.7 Artificial neural network

Although multi-physics simulations can provide accurate information, the computations of the complex internal multi-physics processes are time-consuming, so machine learning methods have been used to facilitate the simulation and optimization process. Artificial neural network (ANN) is a computational model that simulates the operating characteristics of biological neural systems without the need to be aware of the complex relationship of input and output, and has obvious advantages in dealing with complex nonlinear relationships. Numerous studies have demonstrated that ANN is more accurate compared to other prediction algorithms (e.g. Boltzmann machines (BM), decision trees (DT), support vector machines (SVM), etc.) in multi-physics simulations [35]. Fig. 1(b) presents the ANN scheme used in this study. The ANN consists of an input layer, a hidden layer, and an output layer. In this study, the focus is mainly on improving the cell performance and achieving efficient thermal management by adding an in-tube reformer and optimizing the most easily adjustable parameters (operating parameters and reformer structural parameters) without changing the cell structure. Therefore, two structural (radius of anode tube, reformer thickness) and two operating (anode flow rate, glycerol molar fraction) parameters are used as inputs and four performance parameters (current density, system average temperature, electrolyte temperature difference, syngas production) are used as outputs.

252 samples are obtained through Latin hypercube sampling, and a database for training is built using multi-physics simulations. To accelerate convergence, the input data are normalized and scaled to the range [0.1,0.9]:

$$x_{\text{norm}}=0.8\frac{\left(x-x_{\min}\right)}{\left(x_{\max}-x_{\min}\right)}+0.1 \tag{42}$$

where $x_{\max}$ and $x_{\min}$ are the maximum and minimum values of the input, respectively.

The mean square error (MSE) and coefficient of determination (R^2) are used to evaluate the predictive performance of the model:

$$\text{MSE}=\frac{1}{N}\sum_{i=1}^{N}\left(f_i-y_i\right)^2 \tag{43}$$

$$R^2=1-\frac{\sum_{i=1}^{N}\left(y_i-f_i\right)^2}{\sum_{i=1}^{N}\left(y_i-\overline{y_i}\right)^2} \tag{44}$$

where N is the number of samples; y_i and f_i are the predicted and actual values, respectively; and $\overline{y_i}$ is the mean value of y_i.

2.8 Model validation

2.8.1 Model validation for multi-physics model

The calculation is based on a grid of 440000 degrees of freedom (Fig. 2(a)) to achieve a balance between the computational accuracy and solution time. After that, the multi-physics model was validated using experimental results. The electrochemical model was validated through a syngas-fueled button SOFC (Fig. 2(b)) [54]. The chemical model was validated through a glycerol steam reforming fixed-bed reactor (Fig. 2(c)) considering glycerol conversion and H_2 selectivity [44], which are calculated as:

$$\text{Glycerol conversion, } X_{\text{Glycerol}}=\frac{\text{Carbon}_{\text{gas}}}{3\times\text{Glycerol}_{\text{in}}}\times 100\% \tag{45}$$

$$\text{H}_2\text{ selectivity, } S_{\text{H}_2}=\frac{\text{moles of H}_2\text{ in gas products}}{\text{moles of carbon in gas products}}\times\frac{3}{7}\times 100\% \tag{46}$$

The parameters in the model validation are shown in Table 3. From Fig. 2(b) and Fig. 2(c), the numerical results have good agreement with the experimental results.

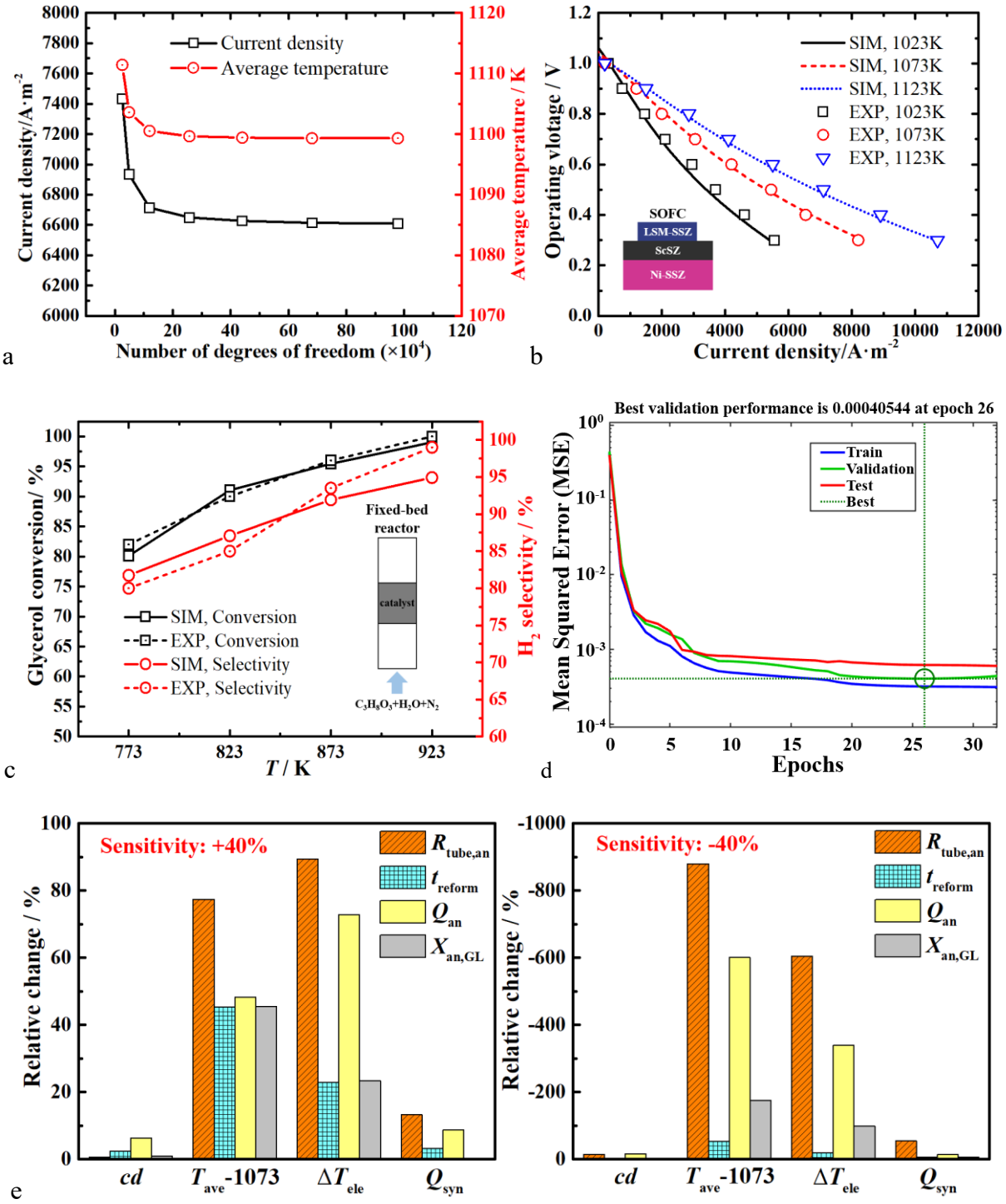

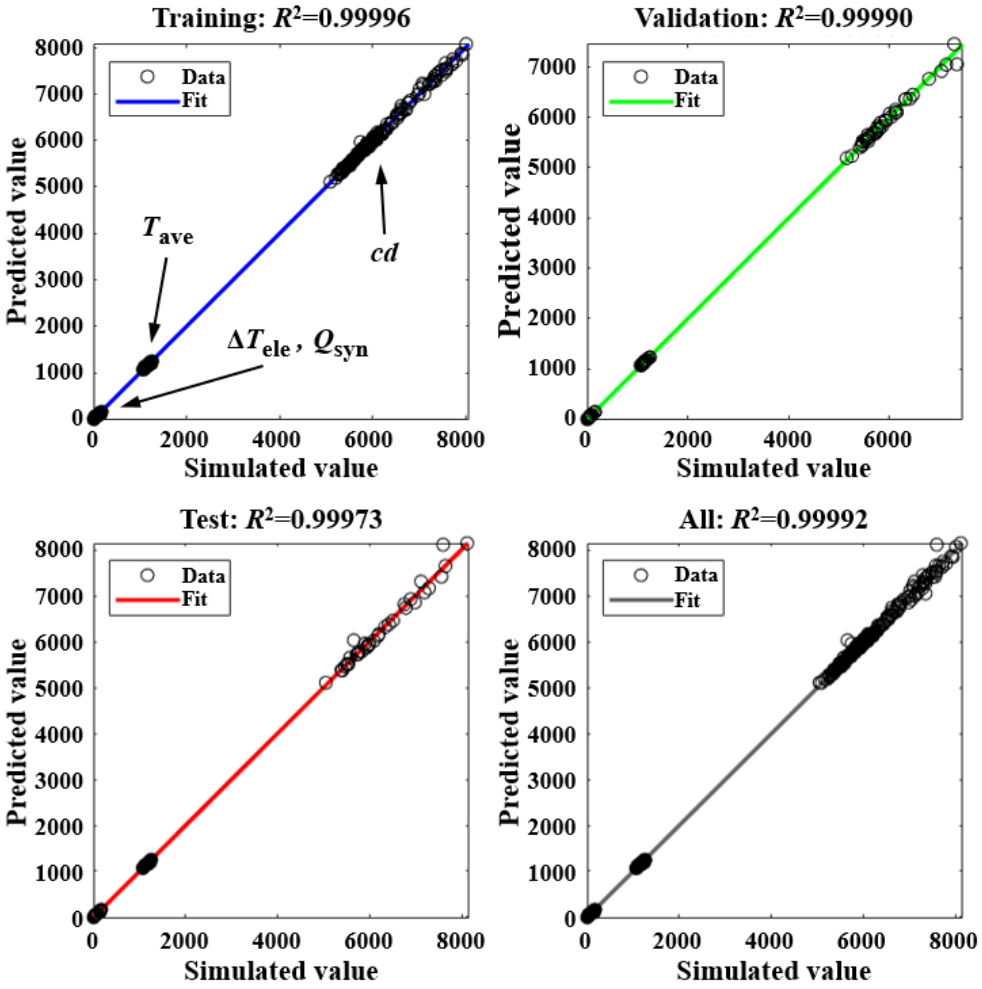

f

Fig.2 (a) Grid independence check; (b) model validation through syngas-fueled button SOFC; (c) model validation through glycerol fixed-bed reactor; (d) mean squared error (MSE) during ANN training; (e) sensitivity analysis for the input parameters of ANN; (f) predicting performance of ANN

Table 3 Parameters in model validation

Parameters	Syngas-fueled button SOFC [54]	Glycerol fixed-bed reactor [44]
Temperature	1023~1123K	773~923K
Voltage	0.3~1.0 V	-
Operating pressure	1 atm	1 atm
Inlet/Anode flow rate	300 SCCM	95 SCCM

Inlet/Anode inlet	H_2:H_2O:CO:CO_2 =19.4%:3.0%:58.2%:19.4%	$C_3H_8O_3$:H_2O:N_2=2%:18%:80%
Cathode flow rate	300 SCCM	-
Cathode inlet	Pure O_2	-

2.8.2 Model validation for ANN

Table 4 demonstrates the detailed features of ANN used in this study. Fig. 2(e) represents the sensitivity analysis for the input parameters (t_{reform}, $R_{tube,an}$, Q_{an}, and $X_{an,GL}$) of ANN. From Fig. 2(e), the average temperature and electrolyte temperature difference are very sensitive to the four input parameters (especially t_{reform} and Q_{an}); while the current density and syngas production are not sensitive due to the relatively large value (5930 $A \cdot m^{-2}$ and 77 SCCM). From Fig. 2(d), the MSE is 4.05×10^{-4}. And Fig. 2(f) represents the prediction ability of ANN for the four performance parameters (current density, system average temperature, electrolyte temperature difference, and syngas production) in this study. It can be seen that for the training set, validation set, test set, and all set, the prediction model has excellent accuracy (R^2 over 0.99, from Fig. 2(f)), indicating that the ANN in this study is well-trained. Table 5 demonstrates the detailed operating conditions used in this study.

Table 4 ANN features in this study

Features	Description
Learning type	Supervised
Architecture	4-10-4
Network topology	Feed-forward
Performance	MSE
Training algorithm	Back-propagation (BP)
Output layer activation function	Linear

Training epochs	100
Number of data used for training/testing/validation	70%:15%:15%

Table 5 Operating conditions in this study [39-42]

Parameters	Value	Unit
Inner radius of anode tube	1.0~1.6	mm
Thickness of in-tube reformer	200~1000	μm
Operating temperature	1073	K
Anode flow rate	50~250	SCCM
Anode tube inlet	$C_3H_8O_3$+H_2O	-
Anode glycerol molar fraction	0.1~0.5	-
Cathode flow rate	300	SCCM
Cathode inlet	Air	-
Operating voltage	0.6	V
Outlet pressure	1	atm

3 Results and discussions

3.1 Effects of in-tube reformer thickness (t_{reform})

Simulations are performed at reformer thickness of 200~1000 μm, with anode tube inner radius of 1.4 mm, anode flow rate of 150 SCCM and glycerol molar fraction of 0.3. To clarify the effect of the in-tube reformer, the same structural (t_{reform}, $R_{tube,an}$) and operating (Q_{an}, $X_{an,GL}$) parameters are used for both the new scheme and old scheme, except that the old scheme does not have a reforming layer in the anode tube. From Fig. 3(a), the addition of the reforming layer in the anode inner tube achieves the pre-reforming of glycerol, which not only increases the glycerol conversion from 62.0% to 82.6% at maximum, but also increases the current density from 5226 $A \cdot m^{-2}$ to 5984 $A \cdot m^{-2}$ due to the increasing H_2 and CO concentration in the anode.

Meanwhile, the sufficient H_2 and CO in the anode channel not only greatly improves the electrochemical reaction and increases the current density at the anode upstream region (x<0.02 m), resulting in a more uniform current density distribution along the stream (Fig. 3(b)), but also increases the H_2 and CO flow rate at the anode outlet, leading to a higher syngas co-production yield (H_2+CO, Fig. 3(c)). It is worth noting that the syngas obtained from the anode co-generation process has a ratio of H_2:CO>2 and a higher yield (Fig. 3(c)), which is suitable as a feedstock for Fischer-Tropsch (F-T) synthesis [55]. Besides, the glycerol pre-reforming process in the anode tube also significantly reduces the temperature gradient inside the cell (Fig. 3(d)) due to the intense heat absorbing glycerol reforming reaction (Eq. (1)). The increasing thickness of the in-tube reforming layer not only moves the system temperature closer to the thermal neutral temperature (1073K), but also reduces the maximum temperature difference of the electrolyte by 74.2% from 21.7 K to 5.6 K when the thickness is 1000 μm (Fig. 3(d)). Moreover, the pre-reforming process in the anode tube can simultaneously absorb excess heat in the anode downstream region (x>0.04 m) and enhance the electrochemical reactions in the anode upstream region (x<0.02 m, by increasing H_2 and CO concentrations in this area). This results in a more uniform temperature distribution along the cell compared to the conventional tubular SOFC, and it becomes more uniform as the reformer thickness increases (Fig. 3(e) and Fig. 3(f)).

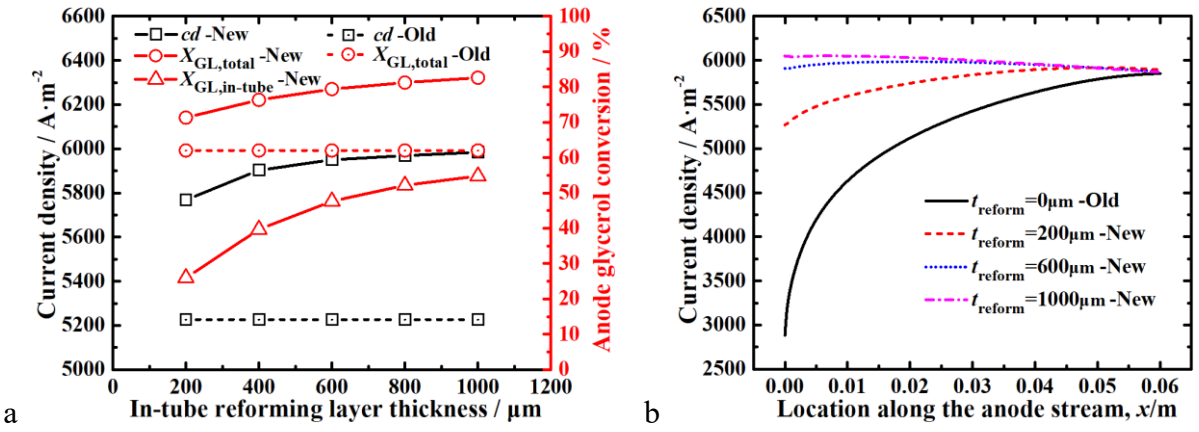

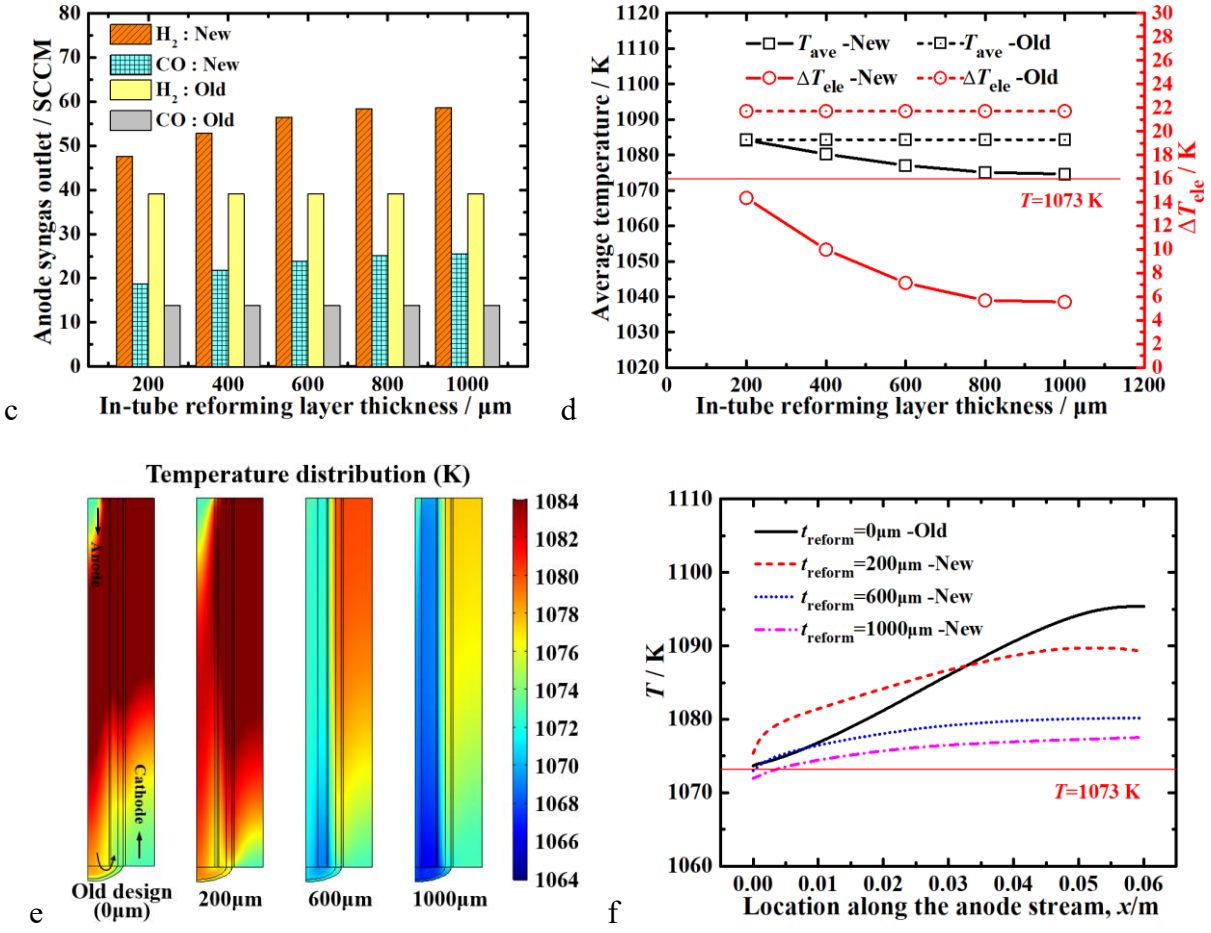

Fig.3 Effects of reformer thickness on: (a) current density and anode glycerol conversion; (b) current density along the electrolyte; (c) anode syngas outlet; (d) average temperature and maximum temperature difference on electrolyte; (e) temperature distribution; (f) temperature distribution along the electrolyte

3.2 Effects of anode tube size ($R_{tube,an}$)

The anode tube is used to support the in-tube reforming layer, with the tube thickness of 0.1 mm. Simulations are performed at anode tube inner radius of 1.0~1.6 mm, with reformer thickness of 600 μm, anode flow rate of 150 SCCM and glycerol molar fraction of 0.3. The increasing inner radius of anode tube reduces the distance between the in-tube reformer and the heat-generating anode, which enhances the heat transfer process and promotes the pre-reforming of glycerol, resulting in higher glycerol conversion and current density (Fig. 4(a)). The increase in current density with in-tube reforming scheme is due to the improved H_2/CO

concentration in the anode channel (especially at x<0.02 m), which avoids the dramatic changes in current density along the cell (Fig. 4(b)) and leads to a higher syngas yield at the anode outlet compared to old configuration (Fig. 4(c)). In addition, the enhanced heat transfer process between the anode and in-tube reformer leads to a significant decrease in the maximum electrolyte temperature difference from 20.6 K to 3.0 K, with a reduction rate of 85.5% at R_{tube}=1.6 mm (Fig. 4(d)). From Fig. 4(e) and Fig. 4(f), the increasing dimension of the anode inner tube can significantly reduce the temperature difference inside the PEN, thus leading to a more uniform temperature distribution along the cell. This can effectively avoid the structural damage and performance failure of the cell due to large temperature gradients and thermal stress [56], which facilitates the long-term stable operation of the SOFC.

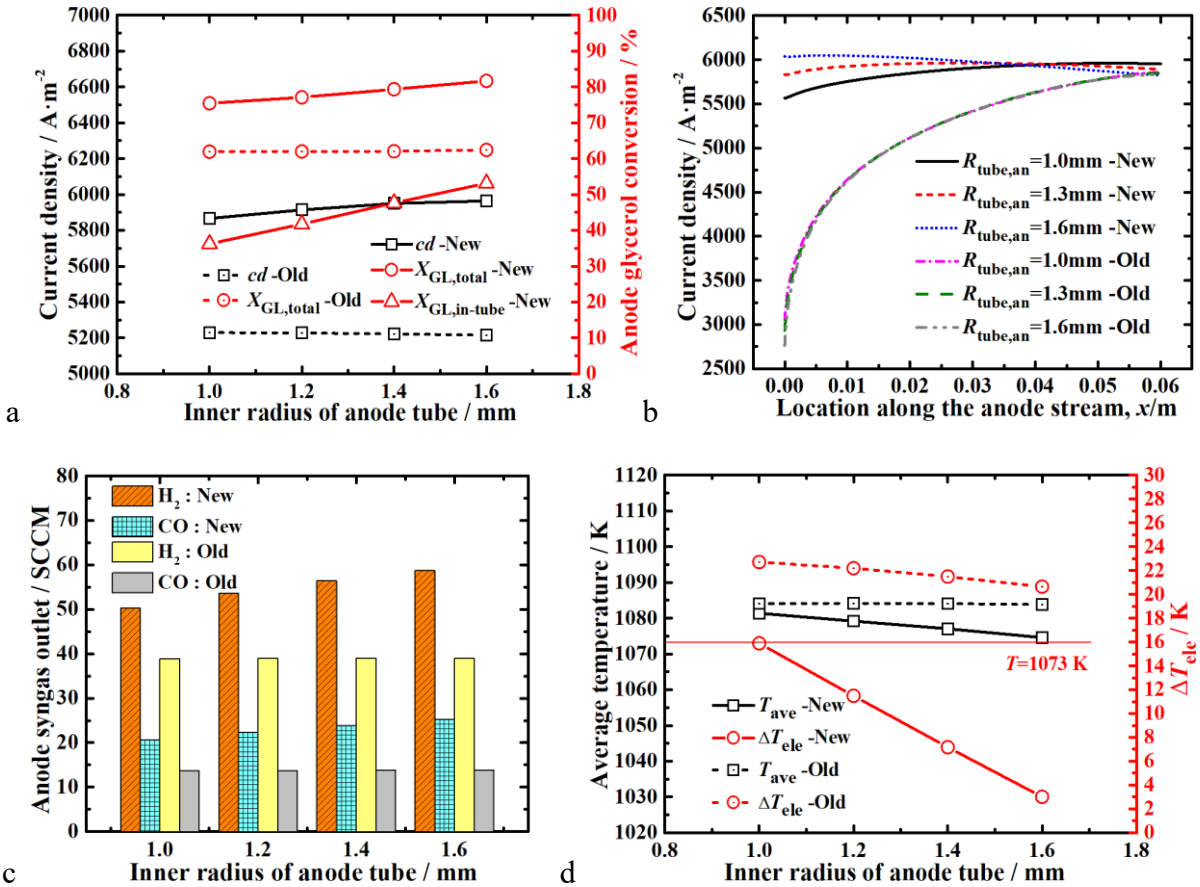

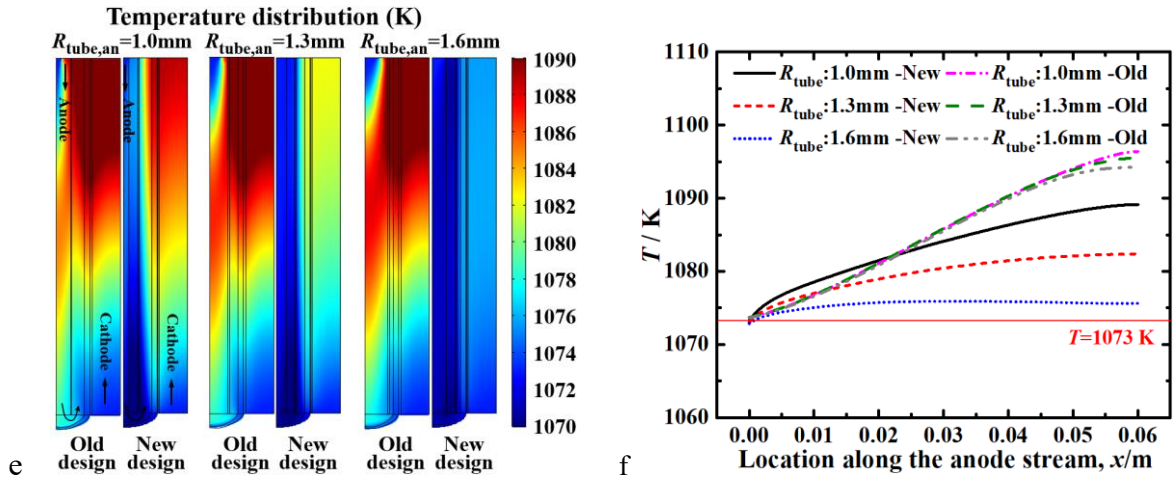

Fig.4 Effects of anode tube inner radius on: (a) current density and anode glycerol conversion; (b) current density along the electrolyte; (c) anode syngas outlet; (d) average temperature and maximum temperature difference on electrolyte; (e) temperature distribution; (f) temperature distribution along the electrolyte

3.3 Effects of anode flow rate (Q_{an})

During operation, a mixture of glycerol and H_2O is supplied into the anode tube to provide fuel (H_2 and CO) for the electrochemical reactions and to control the temperature inside the cell. Simulations are performed at anode flow rate of 50~250 SCCM, anode glycerol molar fraction of 0.3, anode tube inner radius of 1.4 mm, and reformer thickness of 600 μm. At lower anode flow rates (e.g. Q_{an}=50 SCCM), since glycerol is completely converted in the anode inner tube ($X_{GL,in\text{-}tube}$-new=100%), the significantly increased H_2 and CO concentrations in the anode channel and limited reforming heat absorption lead to a remarkable current density increase and a large electrolyte temperature difference (Fig. 5(a), Fig. 5(b), and Fig. 5(d)). As anode flow rate increases, the general tubular SOFC can no longer achieve the complete reforming of glycerol ($X_{GL,total}$-old<100%) due to the increasing quantity of glycerol and the higher anode flow rate (Fig. 5(a)). While the adoption of the in-tube reforming scheme not only brings a 34.2% increase in glycerol conversion (from 43.0% to 57.7%) and 13.5% increase in current density (from 4777 A·m^{-2} to 5420 A·m^{-2} at Q_{an}=250 SCCM, Fig. 5(a)), but also has a

lower electrolyte temperature difference (Fig. 5(d)) and a more uniform temperature distribution along the cell (Fig. 5(e) and Fig. 5(f)). From Fig. 5(c), the increasing anode flow rate not only leads to a higher syngas yield, but also improves the ratio of H_2:CO from 1:1 to 3:1, bring a higher hydrogen content. It is worth noting that when Q_{an} is larger than 200 SCCM, although a uniform along-cell temperature distribution is observed (Fig. 5(f)), the average temperature is less than thermal neutral temperature (Fig. 5(d)) and requires external heat replenishment to maintain stable operation, so excessive flow rate conditions should be avoided.

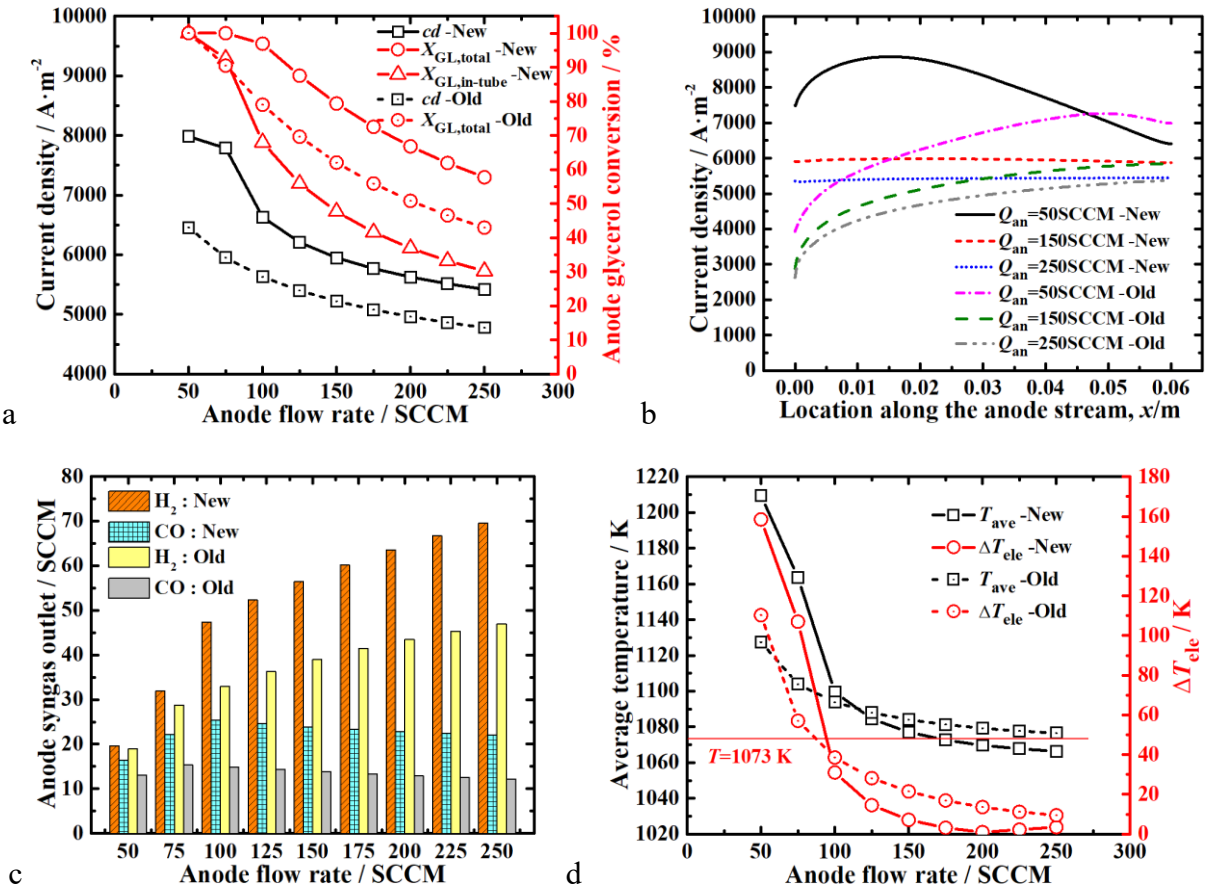

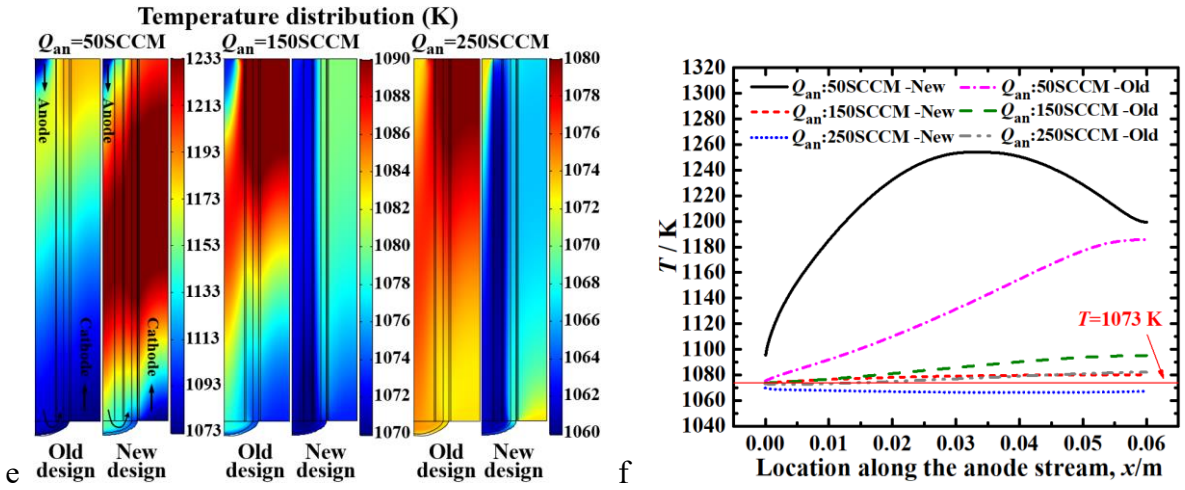

Fig.5 Effects of anode flow rate on: (a) current density and anode glycerol conversion; (b) current density along the electrolyte; (c) anode syngas outlet; (d) average temperature and maximum temperature difference on electrolyte; (e) temperature distribution; (f) temperature distribution along the electrolyte

3.4 Effects of anode glycerol content ($X_{an,GL}$)

Simulations are performed at anode glycerol molar fraction of 0.1~0.5, anode flow rate of 150 SCCM, anode tube inner radius of 1.4 mm, and reformer thickness of 600 μm. At lower glycerol content ($X_{an,GL}$=0.1), glycerol is completely converted to H_2/CO in the in-tube reformer, which greatly facilitates the electrochemical reactions, leading to higher current density and heat generation (Fig. 6(a), Fig. 6(b), and Fig. 6(d)). As the glycerol molar fraction increases, more glycerol is converted and the enhanced heat absorption by glycerol reforming result in a smaller electrolyte temperature difference (Fig. 6(d)). From Fig. 6(a) and Fig. 6(c), when the in-tube pre-reforming scheme is used, it can not only realize a 13.9% increase in current density and 52.0% increase in syngas yield (from 5222 A·m^{-2} and 52.8 SCCM to 5950 A·m^{-2} and 80.2 SCCM at $X_{an,GL}$=0.3, respectively), but also achieve a further reduction of the electrolyte temperature difference from 21.5 K to 7.1 K (Fig. 6(d)), which further improves the uniformity of temperature distribution along the cell compared to the old scheme (Fig. 6(f)).

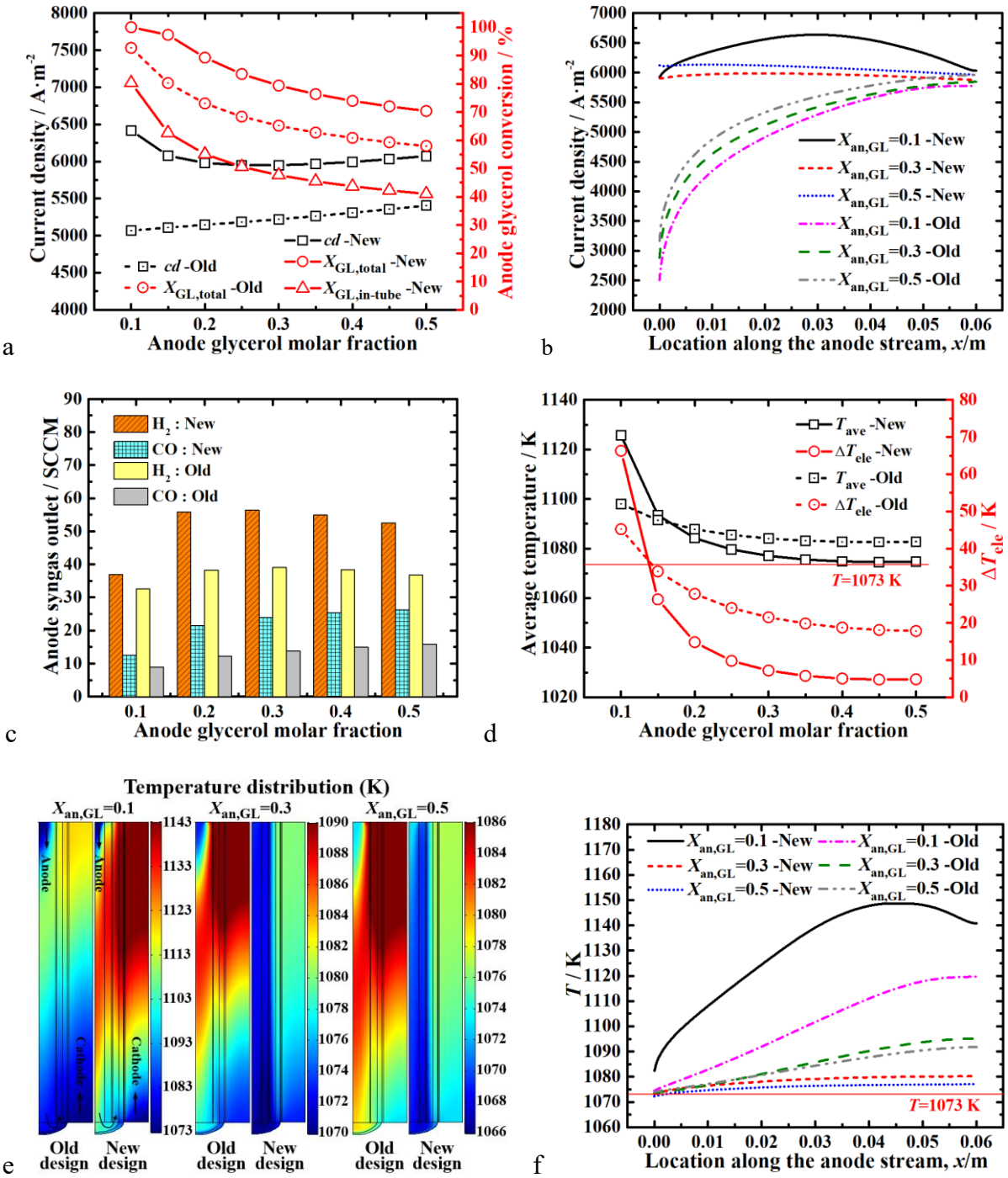

Fig.6 Effects of anode glycerol molar fraction on: (a) current density and anode glycerol conversion; (b) current density along the electrolyte; (c) anode syngas outlet; (d) average temperature and maximum temperature difference on electrolyte; (e) temperature distribution; (f) temperature distribution along the electrolyte

3.5 Multi-objective optimization based on ANN and GA

The analysis of the above parameters shows that the proposed in-tube reforming scheme not only leads to an increasing fuel utilization and current density, but also significantly reduces the maximum PEN temperature difference inside the cell and leads to a more uniform temperature distribution, thus reducing the impact of the large temperature gradient and thermal stress inside the cell effectively. Nevertheless, the output performance and internal temperature distribution of the novel SOFC system are complicated by both the structural (t_{reform}, $R_{\text{tube,an}}$) and operating (Q_{an}, $X_{\text{an,GL}}$) parameters of the in-tube reformer. The MOGA is suitable for solving multi-objective optimization problems in complex nonlinear relationships in SOFC. Therefore, in order to maximize the cell output performance with strict consideration of the thermal effects inside the SOFC, the MOGA is used to predict and optimize the performance based on ANN surrogate model. The optimization in this study focuses on maximizing the output performance and minimizing the PEN temperature difference inside the cell. It is also expected that the cell operates under thermal neutral conditions to eliminate additional heat replenishment/dissipation measures, and also has remarkable co-production performance to produce sufficient syngas. Therefore, the output performance, the maximum electrolyte temperature difference, the system average temperature, and the syngas production are used as the objective functions in the genetic algorithm, and multi-objective optimizations are performed under different operating strategies.

3.5.1 Multi-objective optimization focusing on output performance

The large temperature difference and thermal stress in the PEN can have a serious impact on the long-term stable operation of the cell. Therefore, the output performance and the maximum electrolyte temperature difference are regarded as the key considerations, and the system average temperature is also taken into account to achieve thermal neutral operation ($T_{neutral}$=1073K). This strategy is to achieve maximum output performance with a focus on thermal effects. The MOGA is performed using MATLAB. The genetic algorithm has the

population size of 200 and generations of 500 (exceeding 50 and 400 recommended by MATLAB to ensure accuracy). And the crossover fraction (intermediate crossover) is 0.8, mutation rate (adaptive feasible mutation) is 0.2. The multi-objective optimization issue can be described in Eq. (47), with the same weights set for different objective functions (the weights can be adjusted according to different actual requirements).

$$\begin{cases} \text{Find the optimal solution } X = \left\{ R_{\text{tube,an}}, t_{\text{reform}}, Q_{\text{an}}, X_{\text{an,GL}} \right\} \\ \text{Max } cd, \text{Min } \Delta T_{\text{ele}}, \text{Min abs}\left(T_{\text{ave}} \text{-} T_{\text{neutral}} \right) \end{cases} \tag{47}$$

The corresponding parameter constraints are:

$$\begin{cases} 1.0\text{mm} \le R_{\text{tube,an}} \le 1.6\text{mm} \\ 200\mu\text{m} \le t_{\text{reform}} \le 1000\mu\text{m} \\ 50\text{SCCM} \le Q_{\text{an}} \le 250\text{SCCM} \\ 0.1 \le X_{\text{an,GL}} \le 0.5 \\ V_{\text{cell}} = 0.6\text{V}, T = 1073\text{K} \end{cases} \tag{48}$$

Fig. 7(a) demonstrates the Pareto front under the constraint of current density-maximum temperature difference-average temperature. It can be seen that the maximum current density that can be obtained is about 6000 $\text{A}\cdot\text{m}^{-2}$ under the restriction of minimizing the temperature difference and operating the system in thermal neutral conditions (T=1073K, Fig. 7(a) and Fig. 7(b)). To further increase the current density, compromises have to be made on the maximum temperature difference and system average temperature. With the objective of maximizing the current density and minimizing the temperature difference, the optimal parameters of the GA optimization are $R_{\text{tube,an}}$=1.49 mm, t_{reform}=703 μm, Q_{an}=142 SCCM, and $X_{\text{an,GL}}$=0.46. The current density and syngas production of the optimized system are 6114 $\text{A}\cdot\text{m}^{-2}$ and 80 SCCM, respectively. In order to verify the optimization results of GA, calculations are performed for the optimized new scheme and the old scheme. The same structural (t_{reform}, $R_{\text{tube,an}}$) and operating (Q_{an}, $X_{\text{an,GL}}$) parameters are used for both schemes, except that the old scheme does not have a reforming layer in the anode inner tube. From Fig. 7(c) and Fig. 7(d), the optimized

new scheme has a more uniform temperature distribution compared to the old scheme, which reduces the maximum temperature difference of the electrolyte from 20.0 K to 3.0 K. And the new scheme has a system average temperature of 1073 K and is operated thermal neutrally. Meanwhile, due to the pre-reforming process of glycerol in the in-tube reformer, the H_2 and CO contents in the anode channel and anode outlet are greatly improved (Fig. 7(e)). This significantly improves the electrochemical reactions especially in the anode upstream region (x<0.02 m), increasing the average current density from 5408 A·m^{-2} to 6114 A·m^{-2} (power density from 0.324 W·cm^{-2} to 0.367 W·cm^{-2} at 1073K) and leading to a more uniform current distribution along the cell (Fig. 7(f)).

Typically, a finite temperature gradient is accepted to maximize the output performance of the SOFC during operation. In this case, the maximum output performance and optimal design of the cell under specific temperature constraints can be obtained by simply putting a limit on the maximum temperature difference (e.g. ΔT_{ele}<40K) in Fig. 7(a) and Fig. 7(b). Therefore, the optimization scheme in this study is also applicable to the operating strategies with finite temperature gradients.

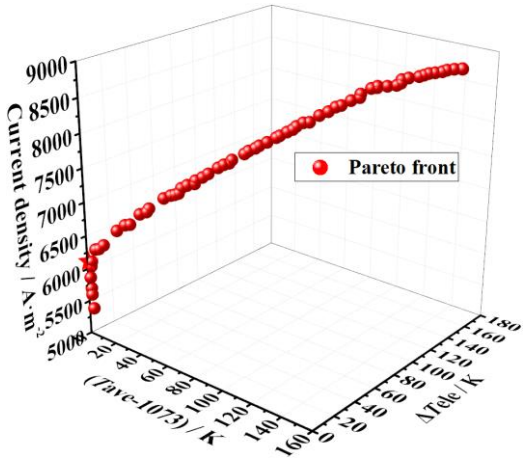

a

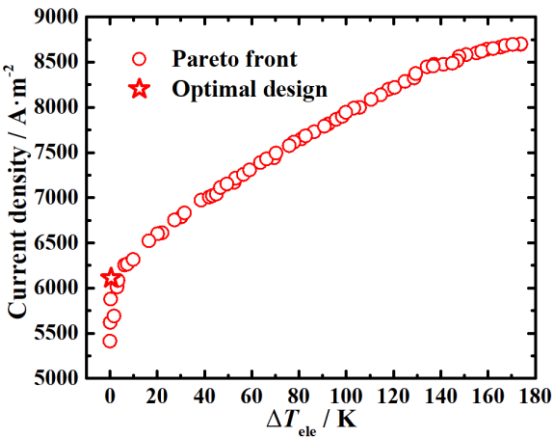

b

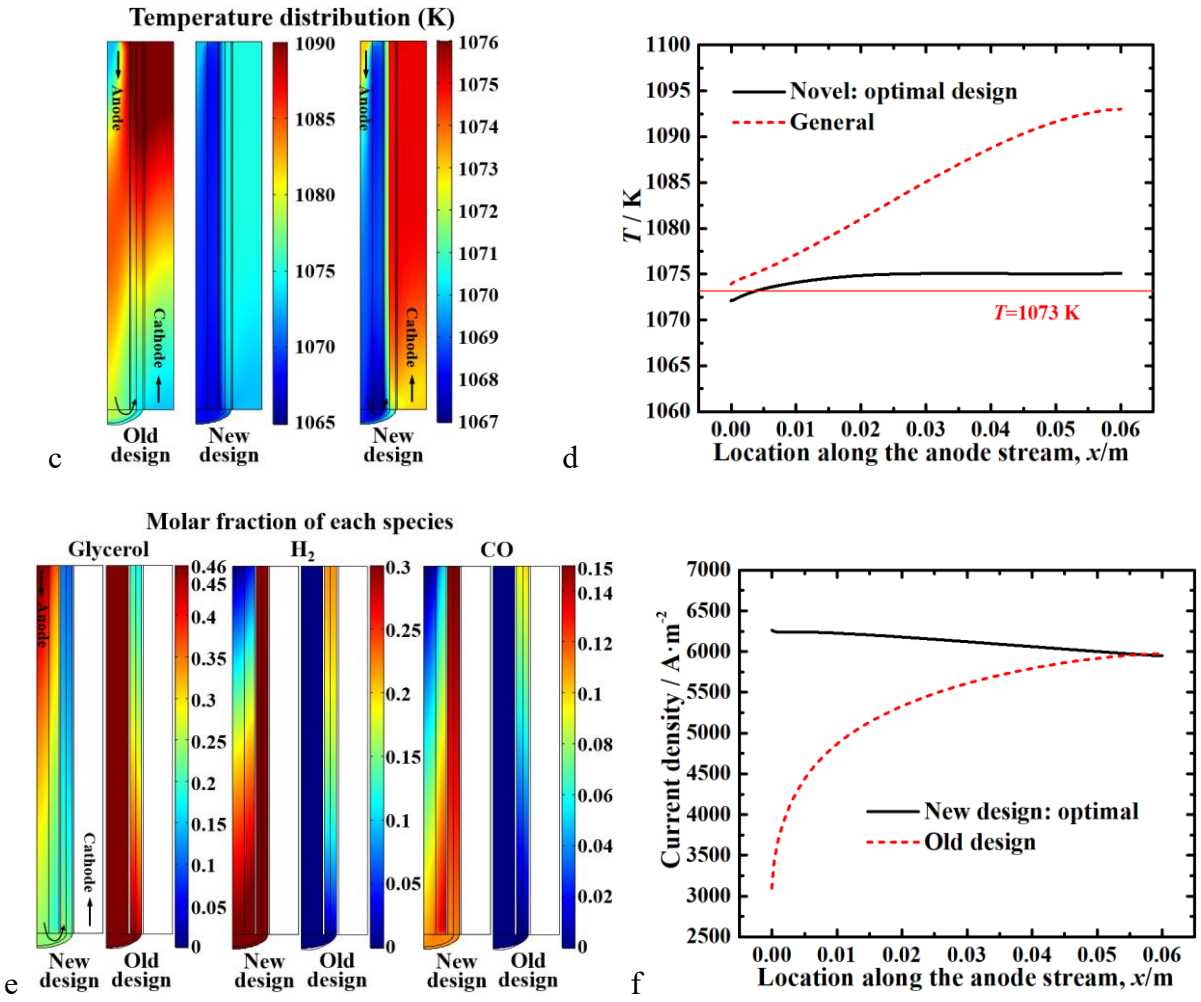

Fig.7 (a) Pareto front in 3D coordinates of current density-maximum temperature difference-system average temperature; (b) Pareto front in 2D coordinates of current density-maximum temperature difference; (c) temperature distribution; (d) temperature distribution along the electrolyte; (e) anode molar fraction of each species; (f) current density distribution along the electrolyte

3.5.2 Multi-objective optimization focusing on syngas production

Since the system can produce electricity and syngas simultaneously, and the H_2 and CO at the anode outlet have a ratio of H_2:CO>2 (suitable for F-T synthesis [55]), this system is also feasible for direct coupling with the F-T synthesis system for subsequent syngas conversion. Therefore, the syngas production is the main objective, and thermal effects are also addressed in order to operate the system thermal neutrally. This strategy is to achieve maximum syngas

production with a focus on thermal effects. The corresponding parameter constraints are shown in Eq. (48). This multi-objective optimization issue can be described is Eq. (49) (same weights set for different objective functions).

$$\begin{cases} \text{Find the optimal solution } X = \left\{ R_{\text{tube,an}}, t_{\text{reform}}, Q_{\text{an}}, X_{\text{an,GL}} \right\} \\ \text{Max } Q_{\text{syn}}, \text{Min } \Delta T_{\text{ele}}, \text{Min abs}\left(T_{\text{ave}} - T_{\text{neutral}} \right) \end{cases} \tag{49}$$

Fig. 8(a) illustrates the Pareto front at the constraints of syngas production-system average temperature, and it is clear that the maximum syngas production of the system is about 86 SCCM under thermal neutral conditions. With the objective of maximizing the syngas production and minimizing the temperature difference, the optimal parameters of the GA optimization are $R_{\text{tube,an}}$=1.50 mm, t_{reform}=996 μm, Q_{an}=198 SCCM, and $X_{\text{an,GL}}$=0.18. The current density and syngas production of the optimized system are 5647 $A \cdot m^{-2}$ and 86 SCCM, respectively. Simulations are performed for the optimized new and old schemes to verify the GA optimization results. From Fig. 8(b), the optimized new scheme has a significant enhancement of H_2 and CO content in the anode channel. Meanwhile, due to the GA optimization of thermal effect, the optimized new scheme can not only operate under thermal neutral conditions (T_{ave}=1073K), but also reduce the maximum electrolyte temperature difference from 19.2 K to 2.3 K, resulting in a more uniform temperature distribution inside the cell (Fig. 8(c) and Fig. 8(d)). Besides, the output performance of the optimized new scheme is also enhanced compared to the old scheme, in which the average current density is not only increased by 16.7% (from 4838 $A \cdot m^{-2}$ to 5647 $A \cdot m^{-2}$), but also eliminates the extremely uneven current distribution inside the cell (Fig. 8(e)).

Therefore, the novel in-tube reformer and the MPS-ANN-MOGA based optimization framework proposed in this study are effective. They can simultaneously increase the SOFC performance and improve the electrochemical/thermal conditions significantly, leading to a uniform current density and temperature distribution along the cell, which facilitates the long-

term stable operation of the SOFC.

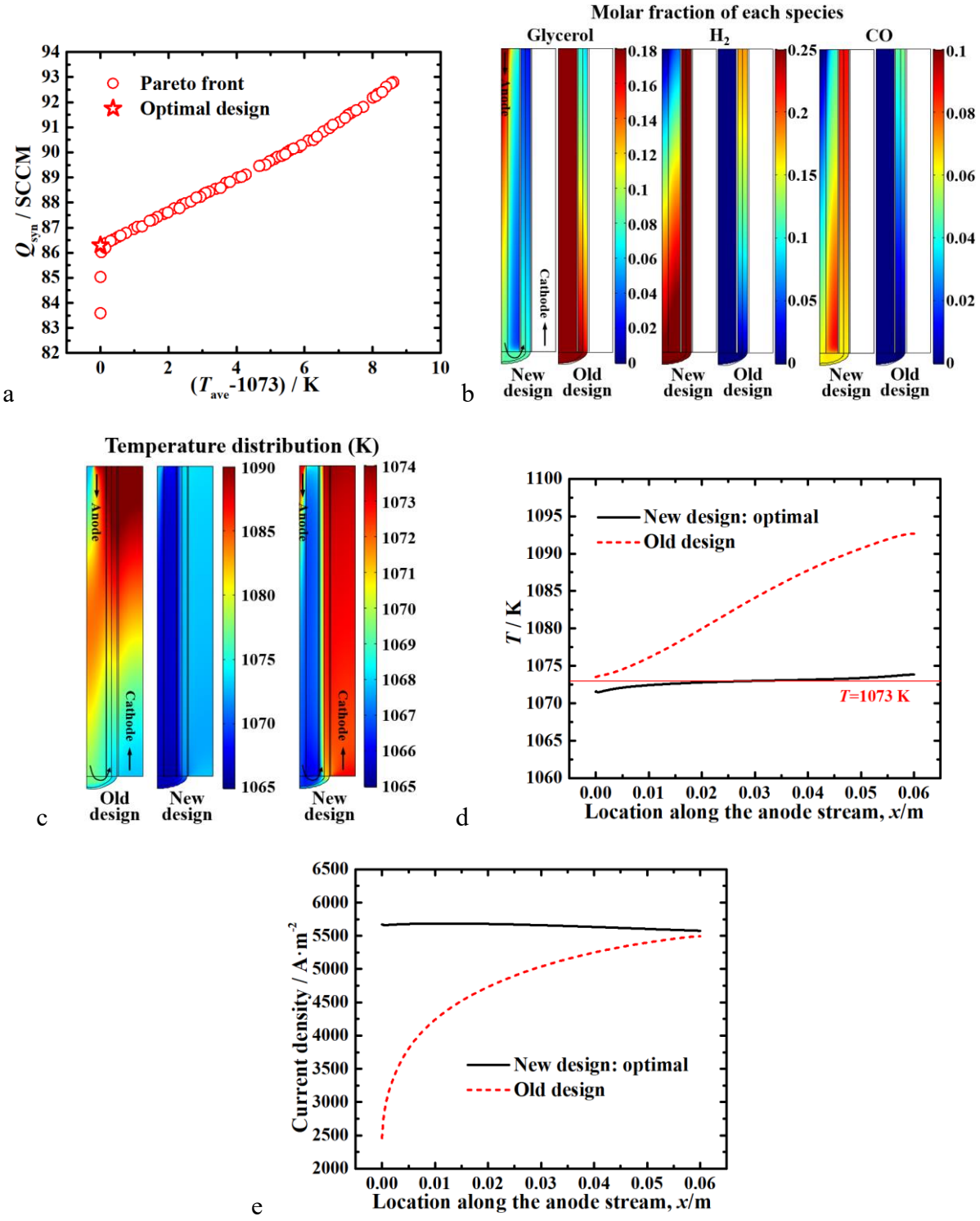

Fig.8 (a) Pareto front in 2D coordinates of syngas production-system average temperature; (b) anode molar fraction of each species; (c) temperature distribution; (d) temperature distribution along the electrolyte; (e) current density distribution along the electrolyte

4 Conclusions

In this study, a novel in-tube reformer is proposed and a MPS-ANN-MOGA based optimization framework is developed to enhance the output performance and reduce the temperature difference within the SOFC. First, a multi-physics model is developed and validated based on experimental data, while the effects of structural (t_{reform}, $R_{tube,an}$) and operating (Q_{an}, $X_{an,GL}$) parameters are analyzed and a database for ANN training is generated. Afterwards, an effective surrogate model with high correlation coefficient is obtained through the training of an artificial neural network, which is used for the accurate prediction of the cell output performance and internal temperature conditions. Finally, multi-objective genetic algorithm optimizations based on the surrogate model are performed under different operating strategies for maximizing the cell performance, eliminating the PEN temperature difference, as well as operating the cell thermal neutrally. The above scheme makes full use of the excess heat in the system to avoid the loss of overall thermal efficiency, and improves the output performance while achieving efficient thermal management of SOFC (eliminating temperature difference and operating in thermal neutrality). The novel in-tube reformer and the optimization framework proposed in this study are demonstrated to be highly powerful and can also be easily applied to other fuel cell/electrolyzer systems to improve system performance and perform efficient thermal management. The main findings and conclusions are as follows:

(1) The use of in-tube reformer allows full use of excess heat in the cell and improves electrochemical reactions, which can increase fuel utilization (by 34.2%) and current density (by 14.5%) while significantly reducing the maximum temperature difference (by 85.4%) in the cell compared to the conventional configuration (without in-tube reformer), resulting in a uniform current density and temperature distribution along the cell.

(2) Small anode flow rate and glycerol content (e.g. Q_{an}=50 SCCM and $X_{an,GL}$=0.1) cause remarkable internal temperature differences, while increasing the reformer thickness, anode

tube size, anode flow rate, and glycerol content improve the uniform distribution of current density and temperature along the cell.

(3) Multi-objective genetic algorithm optimization is performed to obtain the optimal parameters under different operating strategies, which can maximize the performance of the system under efficient thermal management conditions (eliminating temperature difference and operating in thermal neutrality).

Acknowledgements

M. NI thanks the grants (Project Number: N_PolyU552/20) from Research Grants Council, University Grants Committee, Hong Kong SAR.

Reference

[1] Hoogers G. Fuel cell technology handbook[M]. CRC press, Boca Raton, 2002. https://doi.org/10.1201/9781420041552.

[2] Stambouli AB, Traversa E. Solid oxide fuel cells (SOFCs): a review of an environmentally clean and efficient source of energy[J]. Renewable and sustainable energy reviews, 2002, 6(5): 433-455. https://doi.org/10.1016/S1364-0321(02)00014-X.

[3] Nielsen J, Persson ÅH, Muhl TT, et al. Towards high power density metal supported solid oxide fuel cell for mobile applications[J]. Journal of The Electrochemical Society, 2018, 165(2): F90. https://doi.org/10.1149/2.0741802jes.

[4] Develos-Bagarinao K, Ishiyama T, Kishimoto H, et al. Nanoengineering of cathode layers for solid oxide fuel cells to achieve superior power densities[J]. Nature Communications, 2021, 12(1): 3979. https://doi.org/10.1038/s41467-021-24255-w.

[5] Pirou S, Talic B, Brodersen K, et al. Production of a monolithic fuel cell stack with high power density[J]. Nature Communications, 2022, 13(1): 1263. https://doi.org/10.1038/s41467-022-28970-w.

[6] Torrell M, Morata A, Kayser P, et al. Performance and long term degradation of 7 W micro-tubular solid oxide fuel cells for portable applications[J]. Journal of Power Sources, 2015, 285: 439-448. https://doi.org/10.1016/j.jpowsour.2015.03.030.

[7] Monzón H, Laguna-Bercero MA. Highly stable microtubular cells for portable solid oxide fuel cell applications[J]. Electrochimica Acta, 2016, 222: 1622-1627. https://doi.org/10.1016/j.electacta.2016.11.150.

[8] Baldi F, Moret S, Tammi K, et al. The role of solid oxide fuel cells in future ship energy systems[J]. Energy, 2020, 194: 116811. https://doi.org/10.1016/j.energy.2019.116811.

[9] Bessekon Y, Zielke P, Wulff AC, et al. Simulation of a SOFC/Battery powered vehicle[J]. International Journal of Hydrogen Energy, 2019, 44(3): 1905-1918.

https://doi.org/10.1016/j.ijhydene.2018.11.126.

[10] Sumi H, Nakabayashi S, Kawada T, et al. Demonstration of SOFC power sources for drones (UAVs; unmanned aerial vehicles)[J]. ECS Transactions, 2019, 91(1): 149. https://doi.org/10.1149/09101.0149ecst.

[11] Zeng Z, Qian Y, Zhang Y, et al. A review of heat transfer and thermal management methods for temperature gradient reduction in solid oxide fuel cell (SOFC) stacks[J]. Applied Energy, 2020, 280: 115899. https://doi.org/10.1016/j.apenergy.2020.115899.

[12] Cui D, Cheng M. Thermal stress modeling of anode supported micro-tubular solid oxide fuel cell[J]. Journal of Power Sources, 2009, 192(2): 400-407. https://doi.org/10.1016/j.jpowsour.2009.03.046.

[13] Chen B, Xu H, Tan P, et al. Thermal modelling of ethanol-fuelled solid oxide fuel cells[J]. Applied Energy, 2019, 237: 476-486. https://doi.org/10.1016/j.apenergy.2019.01.025.

[14] Akhtar N, Decent SP, Kendall K. Numerical modelling of methane-powered micro-tubular, single-chamber solid oxide fuel cell[J]. Journal of power sources, 2010, 195(23): 7796-7807. https://doi.org/10.1016/j.jpowsour.2010.01.084.

[15] Ni M. Modeling and parametric simulations of solid oxide fuel cells with methane carbon dioxide reforming[J]. Energy Conversion and Management, 2013, 70: 116-129. https://doi.org/10.1016/j.enconman.2013.02.008.

[16] Aguiar P, Adjiman CS, Brandon NP. Anode-supported intermediate temperature direct internal reforming solid oxide fuel cell. I: model-based steady-state performance[J]. Journal of power sources, 2004, 138(1-2): 120-136. https://doi.org/10.1016/j.jpowsour.2004.06.040.

[17] Liu J, Jin F, Yang X, et al. YBaCo2O5+ δ-based double-perovskite cathodes for intermediate-temperature solid oxide fuel cells with simultaneously improved structural stability and thermal expansion properties[J]. Electrochimica Acta, 2019, 297: 344-354.

https://doi.org/10.1016/j.electacta.2018.11.214.

[18] Qi H, Thomas T, Li W, et al. Reduced thermal expansion and enhanced redox reversibility of La0. 5Sr1. 5Fe1. 5Mo0. 5O6− δ anode material for solid oxide fuel cells[J]. ACS Applied Energy Materials, 2019, 2(6): 4244-4254. http://doi.org/10.1021/acsaem.9b00494.

[19] Zhang Y, Chen B, Guan D, et al. Thermal-expansion offset for high-performance fuel cell cathodes[J]. Nature, 2021, 591(7849): 246-251. https://doi.org/10.1038/s41586-021-03264-1.

[20] Zhou C, Shen X, Liu D, et al. Low thermal-expansion and high proton uptake for protonic ceramic fuel cell cathode[J]. Journal of Power Sources, 2022, 530: 231321. https://doi.org/10.1016/j.jpowsour.2022.231321.

[21] Recknagle KP, Williford RE, Chick LA, et al. Three-dimensional thermo-fluid electrochemical modeling of planar SOFC stacks[J]. Journal of Power Sources, 2003, 113(1): 109-114. https://doi.org/10.1016/S0378-7753(02)00487-1.

[22] Fardadi M, McLarty DF, Jabbari F. Investigation of thermal control for different SOFC flow geometries[J]. Applied Energy, 2016, 178: 43-55. https://doi.org/10.1016/j.apenergy.2016.06.015.

[23] Guo M, Zhao D, Xu Q, et al. New interconnector design optimization to balance electrical and mechanical performance of solid oxide fuel cell stack[J]. International Journal of Hydrogen Energy, 2023, 48(8): 3107-3121. https://doi.org/10.1016/j.ijhydene.2022.10.147.

[24] Dillig M, Plankenbühler T, Karl J. Thermal effects of planar high temperature heat pipes in solid oxide cell stacks operated with internal methane reforming[J]. Journal of Power Sources, 2018, 373: 139-149. https://doi.org/10.1016/j.jpowsour.2017.11.007.

[25] Zeng H, Wang Y, Shi Y, et al. Highly thermal integrated heat pipe-solid oxide fuel cell[J]. Applied Energy, 2018, 216: 613-619. https://doi.org/10.1016/j.apenergy.2018.02.040.

[26] Zheng KQ, Sun Y, Shen S, et al. A novel cooler for the thermal management of solid oxide fuel cell stack[J]. Sustainable Energy Technologies and Assessments, 2021, 48: 101564. https://doi.org/10.1016/j.seta.2021.101564.

[27] Promsen M, Komatsu Y, Sciazko A, et al. Feasibility study on saturated water cooled solid oxide fuel cell stack[J]. Applied Energy, 2020, 279: 115803. https://doi.org/10.1016/j.apenergy.2020.115803.

[28] Pajak M, Buchaniec S, Kimijima S, et al. A multiobjective optimization of a catalyst distribution in a methane/steam reforming reactor using a genetic algorithm[J]. international journal of hydrogen energy, 2021, 46(38): 20183-20197. https://doi.org/10.1016/j.ijhydene.2020.02.228.

[29] Pajak M, Brus G, Szmyd JS. Catalyst distribution optimization scheme for effective green hydrogen production from biogas reforming[J]. Energies, 2021, 14(17): 5558. https://doi.org/10.3390/en14175558.

[30] Pajak M, Brus G, Kimijima S, et al. Coaxial multi-criteria optimization of a methane steam reforming reactor for effective hydrogen production and thermal management[J]. Energy and AI, 2023: 100264. https://doi.org/10.1016/j.egyai.2023.100264.

[31] Zaccaria V, Tucker D, Traverso A. Transfer function development for SOFC/GT hybrid systems control using cold air bypass[J]. Applied energy, 2016, 165: 695-706. https://doi.org/10.1016/j.apenergy.2015.12.094.

[32] Nassef AM, Fathy A, Sayed ET, et al. Maximizing SOFC performance through optimal parameters identification by modern optimization algorithms[J]. Renewable energy, 2019, 138: 458-464. https://doi.org/10.1016/j.renene.2019.01.072.

[33] Yan Z, He A, Hara S, et al. Modeling of solid oxide fuel cell (SOFC) electrodes from fabrication to operation: Microstructure optimization via artificial neural networks and multi-objective genetic algorithms[J]. Energy Conversion and Management, 2019, 198:

111916. https://doi.org/10.1016/j.enconman.2019.111916.

[34] Selvam K, Komatsu Y, Sciazko A, et al. Thermodynamic analysis of 100% system fuel utilization solid oxide fuel cell (SOFC) system fueled with ammonia[J]. Energy Conversion and Management, 2021, 249: 114839. https://doi.org/10.1016/j.enconman.2021.114839.

[35] Xu G, Yu Z, Xia L, et al. Performance improvement of solid oxide fuel cells by combining three-dimensional CFD modeling, artificial neural network and genetic algorithm[J]. Energy Conversion and Management, 2022, 268: 116026. https://doi.org/10.1016/j.enconman.2022.116026.

[36] Wang Y, Wu C, Zhao S, et al. Coupling deep learning and multi-objective genetic algorithms to achieve high performance and durability of direct internal reforming solid oxide fuel cell[J]. Applied Energy, 2022, 315: 119046. https://doi.org/10.1016/j.apenergy.2022.119046.

[37] Zhang G, Patuwo BE, Hu MY. Forecasting with artificial neural networks: The state of the art[J]. International journal of forecasting, 1998, 14(1): 35-62. https://doi.org/10.1016/S0169-2070(97)00044-7.

[38] Davis L. Handbook of genetic algorithms[M]. Van Nostrand Reinhold, New York, 1991.

[39] Ni M, Leung MKH, Leung DYC. Parametric study of solid oxide fuel cell performance[J]. Energy Conversion and Management, 2007, 48(5): 1525-1535. https://doi.org/10.1016/j.enconman.2006.11.016.

[40] Xu HR, Chen B, Irvine J, et al. Modeling of CH4-assisted SOEC for H2O/CO2 co-electrolysis[J]. International Journal of Hydrogen Energy, 2016, 41(47): 21839-21849. https://doi.org/10.1016/j.ijhydene.2016.10.026.

[41] Wang C, He QJ, Li Z, et al. Modelling of solid oxide fuel cells with internal glycerol steam reforming[J]. International Journal of Hydrogen Energy, 2022, 47(33): 15012-15023.

https://doi.org/10.1016/j.ijhydene.2022.03.001.

[42] Wang C, Li Z, Zhao SY, et al. Modelling of an integrated protonic ceramic electrolyzer cell (PCEC) for methanol synthesis[J]. Journal of Power Sources, 2023, 559: 232667. https://doi.org/10.1016/j.jpowsour.2023.232667.

[43] Rönsch S, Schneider J, Matthischke S, et al. Review on methanation–From fundamentals to current projects[J]. Fuel, 2016, 166: 276-296. https://doi.org/10.1016/j.fuel.2015.10.111.

[44] Wang Y, Zhu S, Lu J, et al. Boosting hydrogen production from steam reforming of glycerol via constructing moderate metal-support interaction in Ni@ Al2O3 catalyst[J]. Fuel, 2022, 324: 124583. https://doi.org/10.1016/j.fuel.2022.124583.

[45] Li W, Wang H, Shi Y, et al. Performance and methane production characteristics of H2O–CO2 co-electrolysis in solid oxide electrolysis cells[J]. International Journal of Hydrogen Energy, 2013, 38(25): 11104-11109. https://doi.org/10.1016/j.ijhydene.2013.01.008.

[46] Suwanwarangkul R, Croiset E, Fowler MW, et al. Performance comparison of Fick's, dusty-gas and Stefan–Maxwell models to predict the concentration overpotential of a SOFC anode[J]. Journal of Power Sources, 2003, 122(1): 9-18. https://doi.org/10.1016/S0378-7753(02)00724-3.

[47] Veldsink JW, Van Damme RMJ, Versteeg GF, et al. The use of the dusty-gas model for the description of mass transport with chemical reaction in porous media[J]. Chemical Engineering Journal-Including Biochemical Engineering Journal, 1995, 57(2): 115-126. https://doi.org/10.1016/0923-0467(94)02929-6.

[48] Coker AK. Ludwig's applied process design for chemical and petrochemical plants[M]. gulf professional publishing, Houston, Texas, 2014. https://doi.org/10.1016/C2009-0-27075-9.

[49] Liu QG, Ma LX, Liu J. Handbook of Chemistry and Chemical Properties Data (Organic Volume) [M]. Chemical Industry Press, Beijing, 2002.

[50] Todd B, Young JB. Thermodynamic and transport properties of gases for use in solid oxide fuel cell modelling[J]. Journal of power Sources, 2002, 110(1): 186-200. https://doi.org/10.1016/S0378-7753(02)00277-X.

[51] Poling BE, Prausnitz JM, O'Connell JP, et al. The properties of gases and liquids[M]. vol. 12. Mcgraw-hill New York; 2001. https://doi.org/10.1063/1.3060771.

[52] Fuller EN, Ensley K, Giddings JC. Diffusion of halogenated hydrocarbons in helium. The effect of structure on collision cross sections[J]. The Journal of Physical Chemistry, 1969, 73(11): 3679-3685. https://doi.org/10.1021/j100845a020.

[53] Wang C, Li Z, He QJ, et al. Effect of Interconnector Rib on Optimization of SOFC Structural Parameters[J]. Journal of The Electrochemical Society, 2022, 169(9): 094511. https://doi.org/10.1149/1945-7111/ac911d.

[54] Li C, Shi Y, Cai N. Elementary reaction kinetic model of an anode-supported solid oxide fuel cell fueled with syngas[J]. Journal of power sources, 2010, 195(8): 2266-2282. https://doi.org/10.1016/j.jpowsour.2009.10.051.

[55] Dos Santos RG, Alencar AC. Biomass-derived syngas production via gasification process and its catalytic conversion into fuels by Fischer Tropsch synthesis: A review[J]. International Journal of Hydrogen Energy, 2020, 45(36): 18114-18132. https://doi.org/10.1016/j.ijhydene.2019.07.133.

[56] Lin CK, Chen TT, Chyou YP, et al. Thermal stress analysis of a planar SOFC stack[J]. Journal of Power Sources, 2007, 164(1): 238-251. https://doi.org/10.1016/j.jpowsour.2006.10.089.